



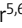





BRIEF DEFINITIVE REPORT

Intestinal epithelial c-Maf expression determines enterocyte differentiation and nutrient uptake in mice

Catalina Cosovanu¹, Philipp Resch¹, Stefan Jordan¹, Andrea Lehmann², Markus Ralser^{2,3}, Vadim Farztdinov⁴, Joachim Spranger^{5,6}, Michael Mülleder⁴, Sebastian Brachs^{5,6}, and Christian Neumann¹

The primary function of the small intestine (SI) is to absorb nutrients to maintain whole-body energy homeostasis. Enterocytes are the major epithelial cell type facilitating nutrient sensing and uptake. However, the molecular regulators governing enterocytes have remained undefined. Here, we identify c-Maf as an enterocyte-specific transcription factor within the SI epithelium. c-Maf expression was determined by opposing Noggin/BMP signals and overlapped with the zoned enrichment of nutrient transporters in the mid-villus region. Functionally, enterocytes required c-Maf to appropriately differentiate along the villus axis. Specifically, gene programs controlling carbohydrate and protein absorption were c-Maf-dependent. Consequently, epithelial cell-specific c-Maf deletion resulted in impaired enterocyte maturation and nutrient uptake, including defects in the adaptation to different nutrient availability. Concomitantly, intraepithelial lymphocytes were less abundant, while commensal epithelial cell-attaching SFB overgrew in a c-Maf-deficient environment, highlighting the close interdependence between the intestinal epithelium, immune system, and microbiota. Collectively, our data identified c-Maf as a key regulator of SI enterocyte differentiation and function, essential for nutrient, immune, and microbial homeostasis.

Introduction

The intestinal epithelium forms the major barrier that separates our body from the external environment. Intestinal epithelial cells (IEC) line the surface of the intestinal epithelium, where they aid the digestion of food and absorption of nutrients, and maintain the symbiotic relationship with commensal microbiota, while protecting the host from pathogens (Peterson and Artis, 2014). To carry out this variety of functions, small intestine (SI) IECs have specialized into distinct IECs lineages e.g., for mucus production (goblet cells), hormone production (enteroendocrine cells), chemosensation (tuft cells), host defense (Paneth cells), and absorption (enterocytes; Peterson and Artis, 2014).

All IECs originate from intestinal stem cells at the base of the crypts. These stem cells constantly give rise to progenitor cells that migrate upward along the villus to terminally differentiate into the various specialized IEC lineages until they are shed from the villus tip 3–5 d later (Baulies et al., 2020). Obviously, this complex process of multilineage differentiation and rapid cell turnover needs to be strictly regulated. Indeed, different signaling

pathways, such as Wnt, Notch, bone morphogenetic protein (BMP), and EGF, were shown to control the maintenance and cell-type specification of intestinal stem cells (Baulies et al., 2020).

The majority of SI IECs are absorptive enterocytes (~80%) that are specialized for metabolic function. To efficiently take up macronutrients from the lumen, enterocytes possess a brush-border structure at their apical side across which nutrients are absorbed (Crawley et al., 2014). Nutrient absorption itself is mediated by the expression and coordinated activity of specific brush-border enzymes and nutrient transporters, which facilitate the terminal digestion and absorption of dietary macromolecules (Hooton et al., 2015).

An important aspect of nutrient absorption is the ability of enterocytes to perceive and dynamically adapt to fluctuating concentrations of different dietary constituents to maximize absorptive efficiency. This adaptation is achieved by dynamically matching the expression of specific types of brush-border

¹Department of Microbiology, Infectious Diseases and Immunology, Charité – Universitätsmedizin Berlin, Berlin, Germany; ²Department of Biochemistry, Charité – Universitätsmedizin Berlin, Berlin, Germany; ³The Francis Crick Institute, Molecular Biology of Metabolism Laboratory, London, UK; ⁴Core Facility - High-Throughput Mass Spectrometry, Charité – Universitätsmedizin Berlin, Berlin, Germany; ⁵Department of Endocrinology and Metabolism, Charité – Universitätsmedizin Berlin, Berlin, Germany; ⁶German Centre for Cardiovascular Research, partner site Berlin, Berlin, Germany.

Correspondence to Christian Neumann: c.neumann@charite.de.

© 2022 Cosovanu et al. This article is distributed under the terms of an Attribution–Noncommercial–Share Alike–No Mirror Sites license for the first six months after the publication date (see <http://www.rupress.org/terms/>). After six months it is available under a Creative Commons License (Attribution–Noncommercial–Share Alike 4.0 International license, as described at <https://creativecommons.org/licenses/by-nc-sa/4.0/>).

enzymes and nutrient transporters to the availability of the respective dietary substrates (Diamond and Karasov, 1987; Mochizuki et al., 2010; Sullivan et al., 2021). Similarly, enterocytes also exhibit regionality in nutrient function along the intestine as well as along the crypt–villus axis (Moor et al., 2018; Seiler et al., 2019; Gebert et al., 2020; Wang et al., 2020; Burclaff et al., 2022). Especially, the spatial differentiation and compartmentalization of enterocytes along the SI villus axis, including the zoned expression of many nutrient transporters, have highlighted the complexity of differentiated enterocytes and their role in nutrient sensing and absorption (Moor et al., 2018; Harnik et al., 2021).

Importantly, although optimal nutrition requires enterocytes to appropriately sense and absorb dietary nutrients, the underlying molecular mechanisms have remained poorly understood. Moreover, enterocyte-mediated nutrient uptake and its interconnection to whole-body metabolism is relevant to a variety of diseases, such as malabsorption/malnutrition syndromes or metabolic disorders, including obesity and type 2 diabetes, which constitute a global health concern (Hoffman et al., 2021). Therefore, identification of the signals and molecular mediators regulating nutrient sensing and absorption have significant therapeutic potential.

The transcription factor c-Maf (encoded by *Maf*) belongs to the AP-1 family of basic region and leucine zipper transcription factors, and has been shown to be involved in the regulation of a broad array of biological processes, including lens and bone development, apoptosis, oncogenesis, and the immune response. As shown by us and others, c-Maf is particularly important for the maintenance of intestinal immune homeostasis by regulating diverse innate and adaptive gut-resident immune cells, such as macrophages, ILC3s, Th17 cells, $\gamma\delta$ T cells, and Foxp3⁺ regulatory T (Treg) cells, both in mouse and human (Kikuchi et al., 2018; Tizian et al., 2020; Parker et al., 2020; Rutz et al., 2011; Aschenbrenner et al., 2018; Zuberbuehler et al., 2019; Neumann et al., 2019; Xu et al., 2018). Recently, *Maf* and *Mafb* expression has also been detected in SI IECs but not functionally explored (Sumigray et al., 2018). Here, we discover a novel role of c-Maf for the differentiation and function of SI enterocytes.

Results and discussion

c-Maf expression specifically marks SI enterocytes of the mid-villus region

To define c-Maf expression throughout the intestinal epithelium, we isolated IECs from distinct intestinal locations (duodenum, jejunum, ileum, caecum, proximal, and distal colon) of naive C57BL/6 mice and stained for c-Maf by flow cytometry. This analysis revealed the presence of a distinct c-Maf-expressing IEC population that was detectable along the small intestine but not in the cecum and colon (Fig. 1, A and B). Immunofluorescence (IF) staining of cross-sections of the SI mucosa confirmed the ubiquitous expression of c-Maf in SI IECs (Fig. 1 C).

To identify the distinct IEC subsets expressing c-Maf in the SI, we costained c-Maf with different IEC subset-specific markers, such as Chromogranin A (ChgA; enteroendocrine cells), DCLK1 (tuft cells), and UEA-1 (goblet and Paneth cells) by

IF. However, ChgA-, DCLK1-, or UEA-1-positive IECs were negative for c-Maf (Fig. 1 D). Moreover, we did not detect c-Maf staining in the crypts of the SI (Fig. 1, C and D), indicating that c-Maf was expressed by IECs other than stem cells, tuft cells, Paneth cells, enteroendocrine cells, and goblet cells. To gain deeper insight into the identity of c-Maf-expressing IECs, we made use of publicly available single-cell RNA sequencing (scRNA-Seq) data from murine SI IECs (Haber et al., 2017). This resource dataset revealed that c-Maf expression specifically marked mature enterocytes (Fig. 1 E). Importantly, the specific expression of c-Maf in SI enterocytes was recently confirmed by different scRNA-Seq studies investigating human IECs (Wang et al., 2020; Burclaff et al., 2022), indicating a conserved function of c-Maf in SI enterocytes across different species.

Based on the emerging concept that enterocytes display a broad spatial and functional compartmentalization along the SI villus axis (Moor et al., 2018), we investigated whether c-Maf also displayed a zoned expression in SI IECs. Strikingly, IF showed that c-Maf exhibited a highly specific expression pattern along the crypt–villus axis. While mid-villus IECs stained strongly positive for c-Maf, crypt/bottom- and tip-villus IECs showed only weak to no c-Maf expression (Fig. 1 F), indicating a distinct position-related function of c-Maf. Importantly, the SI mid-villus region has been shown to be enriched for different nutrient transporters (Moor et al., 2018), especially carbohydrate and amino acid transporters, suggesting a potential role of c-Maf in the nutrient absorption machinery of SI enterocytes.

Intestinal epithelial c-Maf expression is driven by BMP signaling

The abundant expression of c-Maf in SI mid-villus enterocytes raised the question about the specific signals regulating c-Maf. Potential extrinsic signals included microbial and dietary cues, which act on enterocytes from the lumen, or lamina propria (LP)-derived signals, such as cytokines produced by intestinal immune cells. Therefore, we systematically assessed epithelial c-Maf expression in several mouse strains deficient for either microbiota (germ-free mice), immune cells (*Rag2*^{-/-}*Il2rg*^{-/-} mice), or particular cytokines, such as the epitheliotropic cytokine IL-22 (*Il22*^{-/-} mice) and its downstream mediator STAT3 (*Stat3*^{flox/flox} *Villin*^{Cre} mice). We also fasted mice to explore the role of dietary signals for regulation of c-Maf expression. In summary, the absence of none of these extrinsic signals significantly influenced epithelial c-Maf expression (Fig. S1 A).

Next, we tested IEC-intrinsic BMP signaling because BMP activity is highest in the mid-/top-villus region, and BMP was shown to be an upstream regulator of *Maf* proteins during epidermal and lens fiber development (van Eijl et al., 2018; Pandit et al., 2011). Indeed, treatment of small intestinal organoid cultures with recombinant BMP4 resulted in an upregulation of *Maf* along with the BMP target *Id1* (Fig. S1 B). Importantly, additional enhancement of BMP signaling by withdrawal of the BMP-antagonist Noggin from the culture medium (ENR [EGF/Noggin/R-Spondin] vs. ER medium) further increased *Maf* and *Id1* expression (Fig. S1 B).

Thus, epithelial c-Maf expression was determined by the opposing activity of Noggin and BMP signaling. Given that

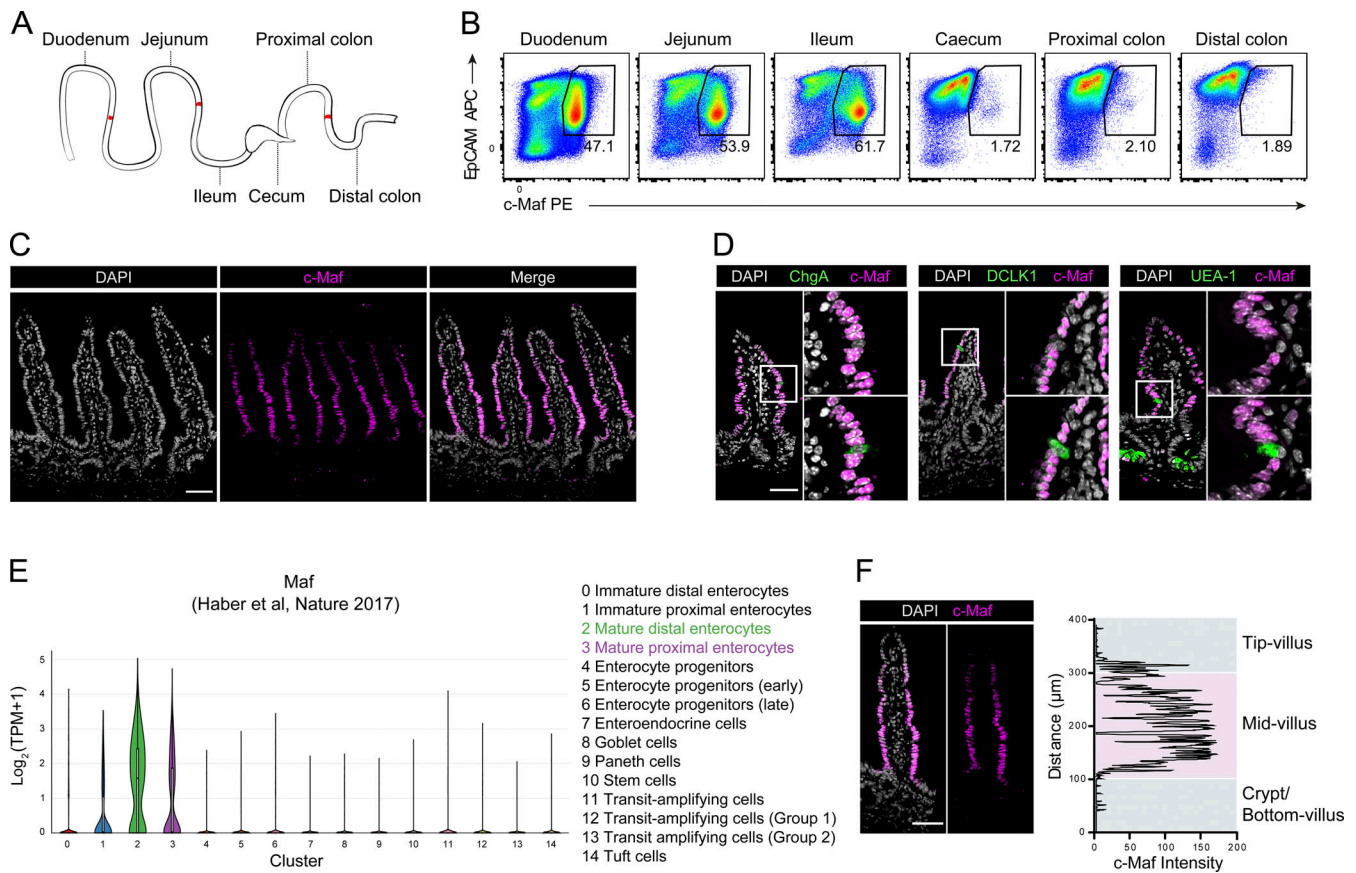


Figure 1. c-Maf expression marks mature SI enterocytes of the mid-villus region. (A) Schematic representation of the murine gastrointestinal tract depicting distinct intestinal segments. (B) Analysis of c-Maf expression in IECs isolated from different intestinal locations of WT C57BL/6 mice. Representative flow cytometric plots of EpCAM vs. c-Maf staining are shown. Pregated on live CD45⁺ cells. Numbers in the plots indicate percentage. (C) Representative IF staining of c-Maf and DAPI on cross-section of the SI of WT C57BL/6 mice. Scale bar, 50 µm. (D) IF co-staining of c-Maf with different secretory IEC marker on cross-section of the SI of WT C57BL/6 mice. Scale bar, 50 µm. (E) *Maf* expression among distinct SI IEC subsets as determined by scRNA-Seq (Haber et al., 2017). (F) Intensity of c-Maf IF staining along the SI crypt-villus axis. Scale bar, 50 µm. Data are representative of at least two independent experiments.

Noggin and BMP form counter gradients at the crypt/villus border, this finding provided a plausible explanation for the specific zoned expression pattern of c-Maf among SI enterocytes. Notably, Suppressor of Mothers against Decapentaplegic (SMAD)-like binding motifs were shown to be enriched in transcriptionally active regions around *Maf* (van Eijl et al., 2018), suggesting that c-Maf expression is directly regulated by BMP/SMAD signaling in enterocytes.

IEC-specific c-Maf-deficient mice show signs of malnutrition

To specifically study the function of c-Maf in IECs, we crossed mice carrying floxed *Maf* alleles to *Villin*^{Cre} mice to generate conditional c-Maf-deficient mice (*Maf*^{flox/flox} *Villin*^{Cre}, referred to as *Maf*^{ΔIEC} hereafter) with a constitutive c-Maf deficiency in villus and crypt epithelial cells of the small and large intestines (El Marjou et al., 2004; Wende et al., 2012). Indeed, analysis of IECs from *Maf*^{ΔIEC} mice by IF and flow cytometry confirmed the absence of c-Maf expression as compared to control animals (Ctrl, *Maf*^{flox/flox}; Fig. 2, A and B).

Generally, *Maf*^{ΔIEC} mice were viable and born in expected Mendelian ratios. However, *Maf*^{ΔIEC} mice appeared smaller and exhibited reduced body weight as compared to their control

littermates (Fig. 2 C). Specifically, the lean body mass, a key parameter of the nutritional status, especially of the somatic protein store (Thibault et al., 2012), was reduced in *Maf*^{ΔIEC} mice (Fig. 2 D). At the same time, the relationship of energy expenditure to lean mass was comparable between *Maf*^{ΔIEC} and control mice (Fig. 2 E), as was the water/food intake (Fig. 2 F), suggesting intestinal malabsorption causing insufficient food efficiency and an overall negative energy balance as the main driver of the reduced nutritional phenotype of *Maf*^{ΔIEC} mice. In agreement with this, *Maf*^{ΔIEC} mice also had a lower body temperature (Fig. 2 G). Consistently, thermogenic interscapular brown adipose tissue (iBAT), but not gonadal white adipose tissue, was reduced in *Maf*^{ΔIEC} mice, and no compensation for the loss of iBAT mass by, e.g., increased thermogenic iBAT activity, as measured by *Ucp1* expression, could be detected in *Maf*^{ΔIEC} mice (Fig. 2, H and I).

The reduced nutritional phenotype of *Maf*^{ΔIEC} mice led us to examine the SI in more detail. Overall, we did not observe substantial differences in SI length and villus architecture in the absence of epithelial c-Maf expression (Fig. 2 J). In line with the absence of c-Maf in secretory IECs, goblet and tuft cell numbers were comparable between *Maf*^{ΔIEC} and control mice (Fig. 2, K

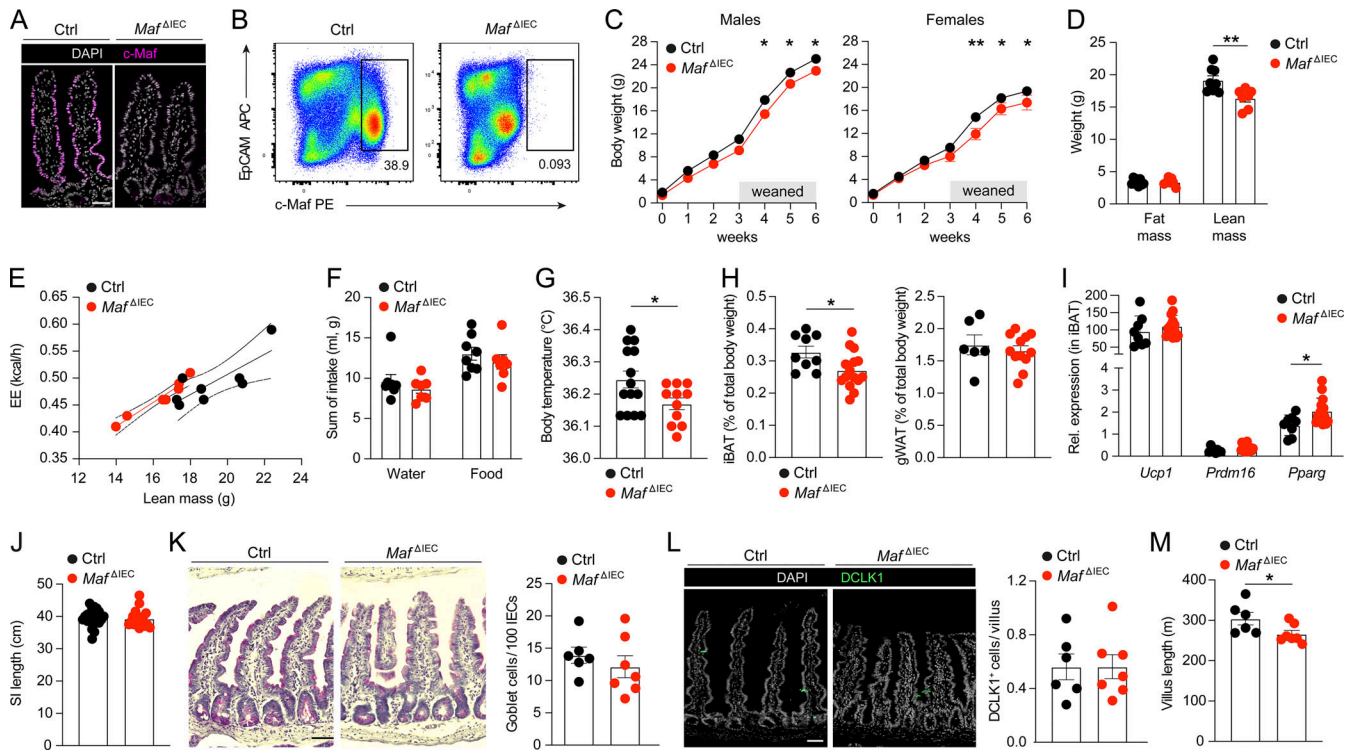


Figure 2. *Maf*^{ΔIEC} mice exhibit a reduced nutritional phenotype. (A) Representative IF staining of c-Maf and DAPI on cross-section of the SI of *Maf*^{ΔIEC} and control mice. Scale bar, 50 μm. (B) Analysis of c-Maf expression in SI IECs from *Maf*^{ΔIEC} and control mice. Representative flow cytometric plots of EpCAM vs. c-Maf staining are shown. Pregated on live CD45⁻ cells. Numbers in the plots indicate percentage. (C) Body weight development over time of male and female *Maf*^{ΔIEC} and littermate control mice (*n* = 6–7 [males], *n* = 3–16 [females], mean ± SEM; *, *P* < 0.05; **, *P* < 0.01). (D) Fat and lean mass of *Maf*^{ΔIEC} and littermate control mice as assessed by NMR (*n* = 7–8, mean ± SEM; **, *P* < 0.01). (E) Regression plot of energy expenditure (EE) vs. lean mass for *Maf*^{ΔIEC} and littermate control mice (*n* = 7–8). (F) Accumulated amount of food and water taken up by *Maf*^{ΔIEC} and littermate control mice over 60 h, two light and three dark phases in metabolic cages (*n* = 7–8, mean ± SEM). (G) Body temperature of 8-wk-old *Maf*^{ΔIEC} and littermate control mice (*n* = 11–14, mean ± SEM; *, *P* < 0.05). (H) Percentage of iBAT and gonadal white adipose tissue (gWAT) of total body weight of *Maf*^{ΔIEC} and littermate control mice (*n* = 6–15, mean ± SEM; *, *P* < 0.05). (I) qPCR analysis of *Ucp1*, *Prdm16*, and *Pparg* expression in iBAT from *Maf*^{ΔIEC} and littermate control mice (*n* = 9–15, mean ± SEM; *, *P* < 0.05). (J) SI length of *Maf*^{ΔIEC} and littermate control mice (*n* = 22–17, mean ± SEM). (K) Representative periodic acid–Schiff staining on cross-section of the SI of *Maf*^{ΔIEC} and control mice. Quantification of goblet cell numbers per 100 IECs (right, *n* = 6–7, mean ± SEM). Scale bar, 50 μm. (L) Representative IF staining of DCLK1 and DAPI on cross-section of the SI of *Maf*^{ΔIEC} and control mice. Quantification of tuft cell numbers per villus (right, *n* = 6–7, mean ± SEM). Scale bar, 50 μm. (M) SI Villus length of *Maf*^{ΔIEC} and littermate control mice (*n* = 6–7, mean ± SEM; *, *P* < 0.05). Data are pooled from at least two independent experiments. Quantification of tuft cells and villus length is based on the analysis of ~100–150 individual villi per mouse. Statistical differences were tested using an unpaired Student’s *t* test (two-tailed).

and L). However, morphometric measurements of villus height revealed shortening of SI villi in *Maf*^{ΔIEC} mice, indicative of a reduced absorptive surface area (Fig. 2 M).

Collectively, these data demonstrated a reduced nutritional phenotype of *Maf*^{ΔIEC} mice, suggesting an important role of c-Maf in controlling the nutrient uptake capacity of SI enterocytes.

c-Maf controls intestinal carbohydrate and protein uptake

To better define the c-Maf-dependent molecular mechanisms underlying the nutritional phenotype of *Maf*^{ΔIEC} mice, we performed RNA-Seq analysis of IECs (CD45⁻ Epcam⁺ cells, sorting strategy see Fig. S2 A) isolated from the SI of *Maf*^{ΔIEC} and control mice. Principal component analysis (PCA) showed that c-Maf-deficient IECs clustered separately from their WT counterparts, demonstrating a unique role of c-Maf in shaping the transcriptome of IECs (Fig. S2 B)

We identified 1,063 genes as differentially expressed (DE; false discovery rate [FDR] <0.1) between c-Maf-deficient and control

IECs, the majority of which (648 genes) were downregulated in the absence of c-Maf (Fig. 3 A and Table S1). This group included several genes involved in intestinal carbohydrate and protein absorption, such as the prominent glucose transporters, *Slc2a2* (GLUT2), *Slc2a5* (GLUT5), and *Slc5a1* (SGLT1); the main peptide transporter *Slc15a1* (PEPT1); and the amino acid transporters *Slc6a19* (B(0)AT1), *Slc7a7* (y+LAT1), *Slc7a8* (LAT2), *Slc7a9* (b(0,+)-AT1), *Slc7a15* (ArpAT), and *Slc16a10* (TAT1; Fig. 3, A and B; and Fig. S2, C and D). We also found many brush-border enzymes responsible for the final stage of carbohydrate and protein digestion, such as *Lct*, *Ace*, *Ace2*, *Anpep*, *Enpep*, *Dpp4*, and *Mme* to be downregulated in c-Maf-deficient IECs (Fig. 3, A and B). Consistently, predefined Kyoto Encyclopedia of Genes and Genomes gene sets for carbohydrate and protein digestion and absorption were significantly downregulated in IECs from *Maf*^{ΔIEC} mice (Fig. 3 C), demonstrating that c-Maf globally governs gene programs of carbohydrate and protein uptake in IECs. Notably, key genes involved in lipid uptake were not differentially regulated in

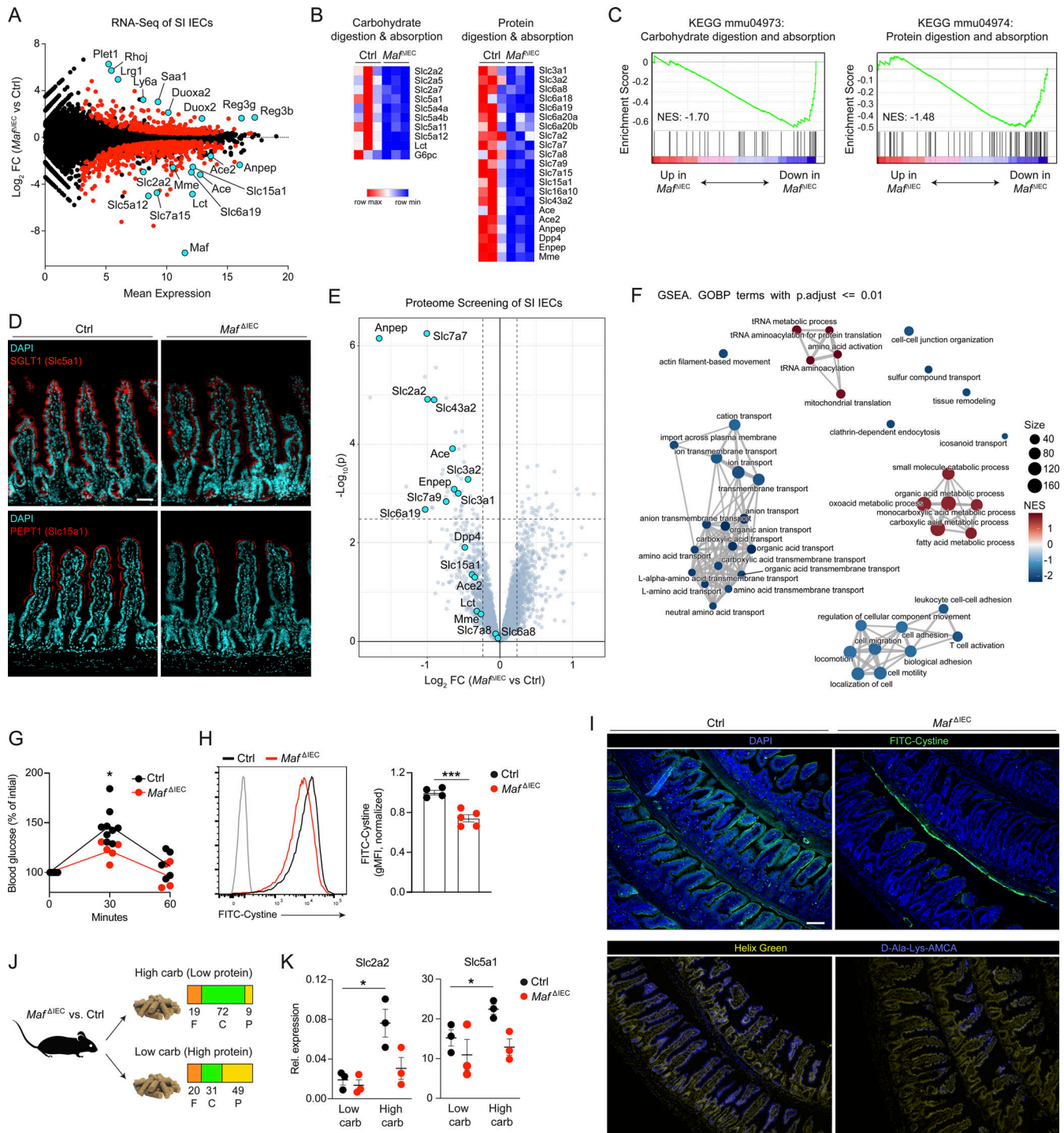


Figure 3. c-Maf controls intestinal nutrient uptake and sensing. (A) CD45⁻ EpCam⁺ IECs were sorted from the SI of $Maf^{ΔIEC}$ and control mice and subjected to RNA-Seq. MA plot showing comparison of gene expression between c-Maf-deficient and control IECs. Data represent the combined analysis of three biologically independent samples. Genes considered significant (FDR < 0.1) are highlighted in red, while selected genes are highlighted in light blue. (B) Heat map plots of genes associated with carbohydrate and protein digestion that are differentially expressed (FDR < 0.1) between $Maf^{ΔIEC}$ and control IECs. (C) Gene set enrichment plots showing downregulation of gene sets associated with carbohydrate and protein digestion in c-Maf-deficient IECs. NES, normalized enrichment score. (D) Representative IF staining of SGLT1 (*Slc5a1*) and PEPT1 (*Slc15a1*) on cross-section of the SI of $Maf^{ΔIEC}$ and control mice. Scale bar, 50 μm . (E) Volcano plot showing comparative of protein expression between c-Maf-deficient and control IECs. Data represent the combined analysis of eight and five biologically independent samples from control and $Maf^{ΔIEC}$ mice, respectively. Proteins involved in carbohydrate or protein uptake, whose corresponding genes showed differential expression in our RNA-Seq data, are highlighted. (F) GSEA of whole proteome comparison between c-Maf-deficient and control IECs with a focus on biological processes (GOBP). The size of each circle represents the weighted number of proteins involved in the term. (G) Increase of blood glucose level after oral administration of glucose following 7 h of fasting ($n = 6$, mean \pm SEM; *, $P < 0.05$). (H) Uptake of FITC-Cystine by primary IECs from $Maf^{ΔIEC}$ and control mice. Representative histogram of FITC-Cystine within CD45⁻ EpCam⁺ IECs (left). Gray peak represents control IECs incubated without FITC-

Cystine. Graph on the right shows quantification of FITC-Cystine geometric mean fluorescence intensity (gMFI). Data are normalized to the mean gMFI of the control samples ($n = 4-5$, mean \pm SEM; ***, $P < 0.001$). **(I)** Representative IF microscopy analysis of ex vivo SI whole-tissue uptake assays with fluorescent Biotracker FITC-Cystine or D-Ala-Lys-AMCA. Scale bar, 100 μ m. **(J)** Scheme depicting feeding of $Maf^{\Delta IEC}$ and control mice with purified diets enriched for carbohydrates (C) or protein (P), F, fat. **(K)** Relative expression of glucose transporters *Slc2a2* and *Slc5a1* by IECs from $Maf^{\Delta IEC}$ and control mice after 3 wk of feeding purified diets with high or low carbohydrate content ($n = 3$, mean \pm SEM; *, $P < 0.05$).

c-Maf-deficient IECs (Fig. S2 E). Importantly, since mRNA-protein correspondence can be poor (Maier et al., 2009), we validated our RNA-Seq data by IF protein staining of SGLT1 and PEPT1, which were both expressed at reduced levels in $Maf^{\Delta IEC}$ mice (Fig. 3 D). Additionally, we performed an unbiased proteome screening of c-Maf-deficient and control IECs, which similarly confirmed the broad downregulation of proteins involved in carbohydrate and protein breakdown and transport (Fig. 3, E and F; and Table S2).

Next, we functionally tested whether the reduction of nutrient absorption-related genes in $Maf^{\Delta IEC}$ mice also translated into an impaired capacity to take up carbohydrates and/or proteins. Indeed, despite normal homeostatic blood glucose levels (Fig. S2 F), $Maf^{\Delta IEC}$ mice exhibited a diminished increase in blood glucose upon oral glucose administration, demonstrating that in vivo intestinal glucose uptake was impaired in these mice (Fig. 3 G).

Similarly, we also checked amino acid concentrations in blood serum as a read-out of in vivo protein uptake. However, systemic amino acid concentrations were not altered in $Maf^{\Delta IEC}$ mice in steady state (Fig. S2 G). Therefore, we tested amino acid uptake with a more simplistic experimental approach. Ex vivo incubation of primary SI IECs with the fluorescently labeled amino acid biotracker FITC-Cystine (Siska et al., 2016), which is preferentially taken up by, e.g., *Slc7a9* (Feliubadalo et al., 2003), showed reduced uptake into c-Maf-deficient IECs compared with controls, as determined by flow cytometry (Fig. 3 H). Likewise, we detected impaired ex vivo uptake of FITC-Cystine into intact SI tissue from $Maf^{\Delta IEC}$ mice by IF (Fig. 3 I). Using the same assay, we also found the fluorescently labeled dipeptide D-Ala-Lys-AMCA to be taken up less efficiently into c-Maf-deficient IECs (Fig. 3 I), which is in agreement with the downregulation of the peptide transporter *Slc15a1* (PEPT1) in $Maf^{\Delta IEC}$ mice (Groneberg et al., 2001). Accordingly, unbiased proteome screening of liver from $Maf^{\Delta IEC}$ mice showed systemic metabolic changes, including the downregulation of “peptide biosynthesis” and “protein translation,” while catabolic processes and lipid handling were increased as compared with controls (Fig. S2 H and Table S2).

Collectively, these data demonstrated that SI enterocytes required c-Maf to globally express gene programs essential for carbohydrate and protein uptake. Consequently, c-Maf deficiency impaired the capacity of SI enterocytes to absorb these essential nutrients.

c-Maf regulates enterocyte adaptation to dietary carbohydrate availability

Enterocytes are capable of dynamically adapting their gene expression profile to different nutrient availability, thereby enabling flexible and efficient nutrient uptake (Diamond and

Karasov, 1987; Sullivan et al., 2021; Mochizuki et al., 2010). Therefore, we asked whether enterocytes also required c-Maf to sense and adapt to selective nutrient availability. Feeding experiments with purified isocaloric diets that were either enriched for carbohydrates (high carb/low protein) or proteins (low carb/high protein) revealed that the adaptive upregulation of prominent glucose transporters (*Slc2a2*, *Slc5a1*) in response to high dietary carbohydrate availability was abrogated in the absence of c-Maf (Fig. 3, J and K; Sullivan et al., 2021). In contrast, despite being consistently downregulated in $Maf^{\Delta IEC}$ mice, the expression of several peptides and amino acid transporters was largely unaffected by dietary protein availability, as previously shown (Fig. S3 A; Sullivan et al., 2021). We also did not detect changes in c-Maf expression itself upon differential carbohydrate/protein feeding (Fig. S3 B).

The “on demand” induction of the carbohydrate absorptive machinery was recently shown to depend on a complex interplay between IEC and intestinal immune cells, in which the epithelial expression of glucose transporters is indirectly regulated by $\gamma\delta$ T cells via IL-22 produced by ILC3s (Sullivan et al., 2021). Based on this concept, we explored whether epithelial c-Maf deficiency somehow affected this IEC-lymphocyte circuit. However, immune cell phenotyping of SI LP lymphocytes did not show quantitative differences in $\gamma\delta$ T cells and ILC3s, as well as in ILC3-derived IL-22 production between $Maf^{\Delta IEC}$ mice and littermate controls (Fig. 4, A and B). We also did not detect differences in other major SI LP immune cell types, such as Foxp3⁺ regulatory T cells, Th17 cells, and IgA⁺ plasma cells in $Maf^{\Delta IEC}$ mice (Fig. 4 C), excluding a major contribution of immune cell-derived signals to the impaired expression of nutrient transporters in $Maf^{\Delta IEC}$ mice.

Yet, we found intraepithelial lymphocytes (IELs) to be less abundant within the c-Maf-deficient epithelium (Fig. 4 D), indicating an unexpected role of c-Maf-expressing enterocytes in maintaining the SI IEL pool. Further characterization of $Maf^{\Delta IEC}$ IELs did not reveal differences in subset composition (Fig. 4 E, gating strategy in Fig. S3 C) or expression of genes determining cell proliferation and survival (Fig. S3 D). However, the IEL chemoattractant *Cx110* was significantly downregulated in c-Maf-deficient IECs (Table S1; Shibahara et al., 2001), suggesting defects in IEL recruitment in $Maf^{\Delta IEC}$ mice. Functionally, $Maf^{\Delta IEC}$ IELs exhibited reduced expression of *Grzmb*, but not of *Ifng*, *Tnfa*, and *Ili7*, as compared to IELs from controls (Fig. 4 F and Fig. S3 E).

In summary, our data identified c-Maf as a central regulator of the molecular adaptation of SI enterocytes to the nutritional environment. Importantly, homeostatic intestinal immunity was largely uncompromised by epithelial c-Maf deficiency, except for SI IELs, which were quantitatively and qualitatively reduced in $Maf^{\Delta IEC}$ mice.

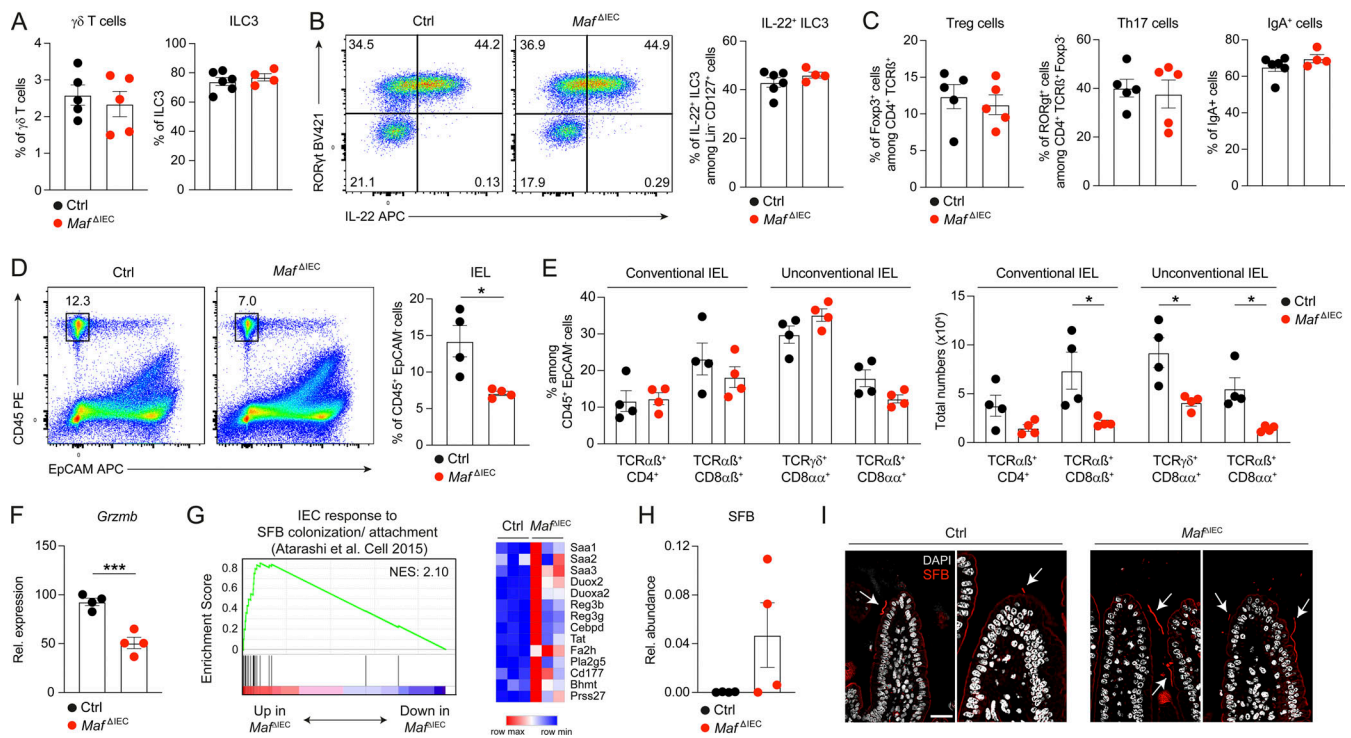


Figure 4. Epithelial c-Maf deletion affects IELs and SFB colonization. (A) Frequency of $\gamma\delta$ T cells among CD45⁺ SI LP lymphocytes and ILC3s among Lin⁻ CD127⁺ cells of *Maf*^{ΔIEC} and control mice ($n = 4$, mean \pm SEM). (B) Frequency of IL-22⁺ ILC3s among Lin⁻ CD127⁺ cells of *Maf*^{ΔIEC} and control mice after ex vivo restimulation with PMA/ionomycin and IL-23. Representative flow cytometric profiles are shown on the left; quantification on the right ($n = 4-6$, mean \pm SEM). Numbers in the plots indicate percentage. (C) Frequency of SI LP Treg cells (CD4⁺ TCR β ⁺ Foxp3⁺), Th17 cells (CD4⁺ TCR β ⁺ Foxp3⁻ ROR γ t⁺), and IgA⁺ cells in *Maf*^{ΔIEC} and control mice ($n = 5$, mean \pm SEM). (D) Frequency of SI IELs (CD45⁺ Epcam⁻) from *Maf*^{ΔIEC} and control mice. Representative flow cytometric profiles are shown on the left; quantification on the right ($n = 4$, mean \pm SEM; *, $P < 0.05$). Numbers in the plots indicate percentage. (E) Frequency and total numbers of different SI IEL subsets from *Maf*^{ΔIEC} and control mice ($n = 4$, mean \pm SEM; *, $P < 0.05$). (F) qPCR analysis of *Grzmb* expression in FACS-sorted SI IELs ($n = 4$, mean \pm SEM; ***, $P < 0.001$). (G) Gene set enrichment and heat map plot showing upregulation of genes induced in IECs upon SFB colonization and attachment in c-Maf-deficient IECs (Atarashi et al., 2015). NES, normalized enrichment score. (H) qPCR analysis of SFB abundance in ileal mucosal samples from *Maf*^{ΔIEC} and control mice. (I) Representative bacterial FISH staining of SFB on cross-section of the ileum of *Maf*^{ΔIEC} and control mice. Scale bar, 20 μ m. Data are representative of or pooled from at least two independent experiments. Statistical differences were tested using an unpaired Student's *t* test (two-tailed).

Aberrant expansion of commensal segmented filamentous bacteria (SFB) in IEC-specific c-Maf-deficient mice

As diet and nutrition have emerged as pivotal determinants of gut microbiota composition (Dahl et al., 2020), we wondered whether the c-Maf-dependent defects in enterocyte nutrient sensing and uptake also affected intestinal microbial homeostasis in *Maf*^{ΔIEC} mice. Indeed, our RNA-Seq data from c-Maf-deficient IECs (Fig. 3 A) revealed a striking upregulation of genes linked to SFB colonization and attachment to IECs, such as *Saa1*, *Saa2*, *Saa3*, *Duox2*, *Duoxa2*, *Reg3g*, and *Cebpd* (Fig. 4 G; Atarashi et al., 2015). Indeed, quantitative PCR (qPCR) from ileal mucosal samples and bacterial FISH analysis demonstrated a substantial increase in the abundance of SFB in *Maf*^{ΔIEC} mice (Fig. 4, H and I). Interestingly, SFB in *Maf*^{ΔIEC} mice also showed differences in morphology, exhibiting long segmented filaments, while SFB in control animals had fewer segments and appeared stubble-like (Fig. 4 I).

Thus, intestinal epithelial c-Maf expression was also essential for the containment of a key commensal bacterium, which has coevolved to intimately associate with the gut epithelium. Due to their reduced genome, SFB are known to highly depend on their

host for essential nutrients (Sczesnak et al., 2011; Prakash et al., 2011; Kuwahara et al., 2011). Therefore, superior access to luminal nutrients caused by incomplete nutrient uptake in *Maf*^{ΔIEC} mice might serve as an explanation for the overgrowth of SFB.

c-Maf deficiency perturbs the spatial differentiation and maturation of enterocytes

Despite the downregulation of genes involved in nutrient uptake, our RNA-Seq data showed that c-Maf deficiency also globally perturbed the differentiation and functional zonation of SI enterocytes (Moor et al., 2018; Harnik et al., 2021). Zonation clusters based on the spatial gene expression profiles of enterocytes along the SI villus axis were significantly dysregulated in *Maf*^{ΔIEC} mice (Fig. 5 A; Moor et al., 2018). Specifically, crypt- and bottom-villus gene clusters (cluster 1 and 2) were upregulated, whereas mid- and top-villus gene clusters (cluster 3 [including c-Maf], 4, and 5) were downregulated in *Maf*^{ΔIEC} IECs (Fig. 5 A). Importantly, the de-enrichment of mid- and top-villus gene clusters was paralleled by downregulation of signature genes for mature enterocytes, whereas genes specific for immature enterocytes were upregulated in IECs from *Maf*^{ΔIEC} mice (Fig. 5 B; Haber et al., 2017). Thus,

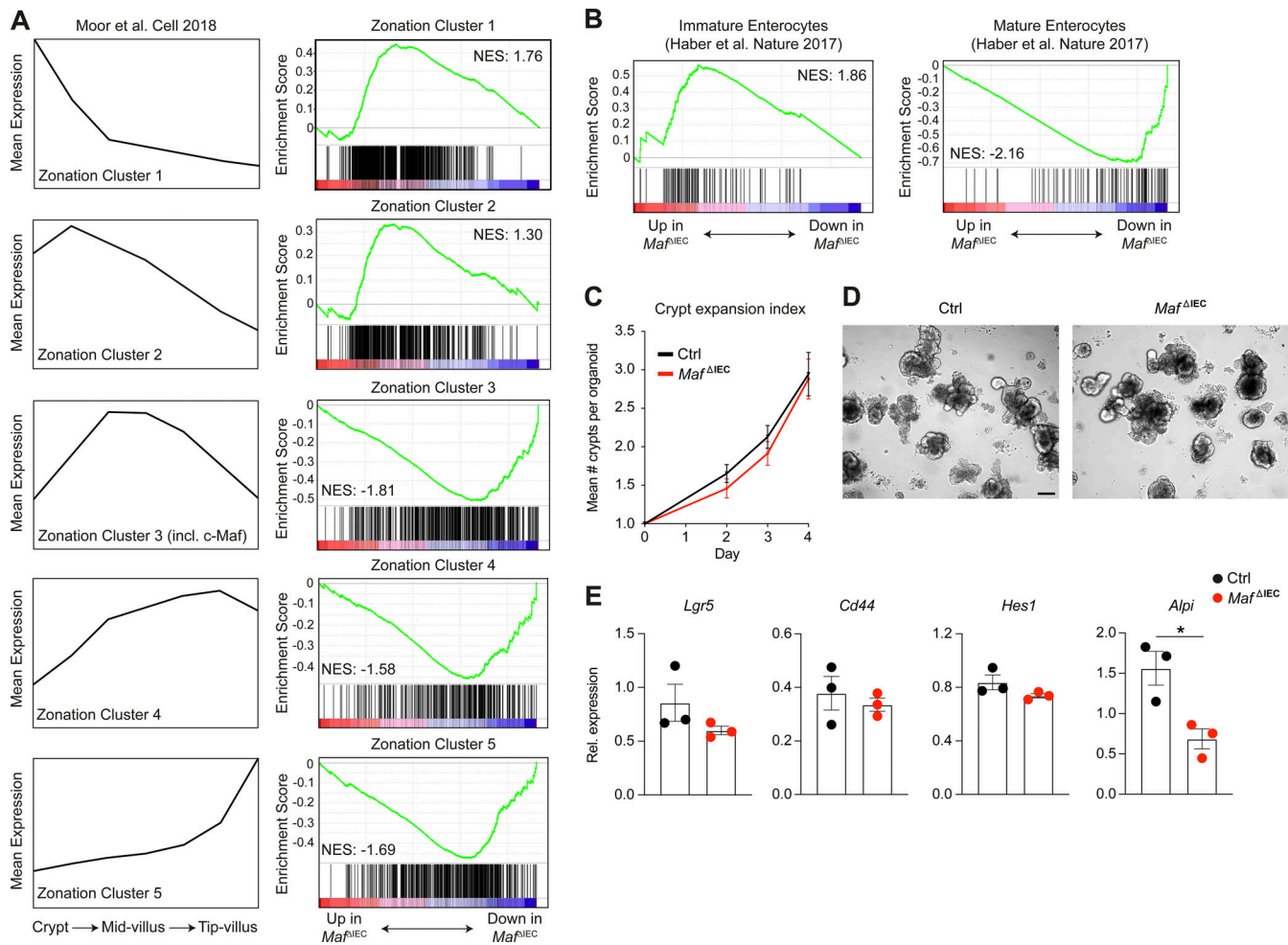


Figure 5. c-Maf governs the spatial differentiation and maturation of enterocytes. (A) Left panel: Visualization of zonation clusters based on the spatial gene expression profiles of enterocytes along the crypt–villus axis (Moor et al., 2018). Right panel: Gene set enrichment plots showing up- or downregulation of zonation clusters in c-Maf-deficient IECs. NES, normalized enrichment score. (B) Gene set enrichment plots showing up- and downregulation of genes specific for immature and mature enterocytes, respectively, in c-Maf-deficient IECs (Haber et al., 2017). (C) Quantification of crypts per organoid over time during SI organoid cultures from *Maf^{ΔIEC}* and control mice ($n = 3$, mean \pm SEM). (D) Representative microscopy pictures of SI organoids from *Maf^{ΔIEC}* and littermate control mice at day 4 of culture. Scale bar, 100 μ m. (E) qPCR analysis of *Lgr5*, *Cd44*, *Hes1*, and *Alpi* expression by SI organoids from *Maf^{ΔIEC}* and littermate control mice at day 4 of culture ($n = 3$, mean \pm SEM; *, $P < 0.05$). Data are representative of or pooled from at least two independent experiments. Statistical differences were tested using an unpaired Student's *t* test (two-tailed).

SI enterocytes required c-Maf expression to appropriately mature and differentiate along the villus axis. In the absence of c-Maf, enterocytes exhibited an impaired maturation status and spatial transcriptome that was characterized by a shift toward immature enterocyte and crypt/bottom-villus gene clusters at the expense of mature enterocyte and mid-/top-villus gene profiles.

The perturbations in enterocyte maturation and zonation in *Maf^{ΔIEC}* mice prompted us to analyze the role of c-Maf for enterocyte differentiation more closely. In vitro modeling of IEC differentiation using small intestinal organoids demonstrated that c-Maf was dispensable for overall organoid growth, and viability as assessed by crypt expansion and morphology of c-Maf-deficient and control organoids (Fig. 5, C and D). Further, qPCR analysis of organoids confirmed the broad downregulation of carbohydrate and protein transporters in the absence of c-Maf, supporting a cell-intrinsic and direct role of c-Maf in the regulation of these genes (Fig. S3, F and G). Consistent with the

absence of c-Maf expression in epithelial crypts, c-Maf-deficient organoids showed unaltered expression of stem cell-related genes, *Lgr5* and *Cd44* (Fig. 5 E). However, we detected diminished expression of *Alpi*, a marker for mature enterocytes, while *Hes1*, which labels absorptive progenitor cells, was not differentially expressed in *Maf^{ΔIEC}* organoids (Fig. 5 E).

Collectively, these results indicated that c-Maf was essential to license SI enterocyte maturation and differentiation. Without c-Maf, enterocytes remained in an immature state and exhibited a skewed zonation profile. Accordingly, a recent study by Petrova and colleagues in this issue similarly reported a role for c-Maf in maintaining enterocyte zonation (González-Loyola et al., 2022). Interestingly, in their study, inducible deletion of c-Maf in IECs in adult mice additionally disrupted the balance between SI enterocytes and secretory cell types, thereby impairing the regenerative epithelial response to acute intestinal injury.

Thus, overall, the precisely timed BMP-mediated upregulation of c-Maf expression in newly formed enterocytes exiting the crypt represents a key step in their developmental trajectory. In this manner, c-Maf facilitates the spatial and functional specialization of enterocytes, including the acquisition of gene programs controlling intestinal nutrient uptake.

Materials and methods

Mice

To generate conditional c-Maf-deficient mice (*Maf^{ΔIEC}*), *Vil-Cre* mice (Madison et al., 2002; kindly provided by A. Diefenbach, Berlin, Germany) were crossed to *Maf-flox* mice (Wende et al., 2012; own breeding). *Rag2^{-/-}Il2rg^{-/-}*, *Il22^{-/-}*, and *Stat3^{flox/flox}* *Villin^{Cre}* mice were also kindly gifted by A. Diefenbach, Berlin, Germany. Germ-free mice were kindly provided by Ahmed Hegazy, Berlin, Germany. All mice were on a C57BL/6 background and bred and maintained under specific pathogen-free conditions at our animal facilities (FEM Charité Berlin, Germany). All mice used were 7–10 wk old. Body weight and temperature were determined using a laboratory scale and an infrared thermometer (FT-100C). All animal experiments were in accordance with the ethical standards of the institution or practice at which the studies were conducted and were reviewed and approved by the responsible ethics committees of Germany (LAGeSo).

Nuclear magnetic resonance (NMR) analysis

For the determination of body composition, fat and lean mass were assessed by 1H-magnetic resonance spectroscopy using a Minispec LF50 Body Composition Analyzer (Bruker BioSpin).

Indirect calorimetry analysis

Basal metabolic parameters were analyzed in a TSE LabMaster System (TSE Systems). Mice were acclimated to the metabolic cages individually housed 8 h before starting and supplied with regular diet. Data on gas exchanges, activity, and food/water intake were collected for 60 h, two light and three dark phases, and analyzed as average over 24 h. Calorimetry was performed with a computer-controlled open circuit calorimetry system composed of 10 metabolic cages. Each cage was equipped with a special water bottle and a food tray connected to a balance as well as an activity monitor. Parameters were measured for each mouse at 2.42-min intervals, and respiratory quotient was calculated as the ratio of CO₂ production to O₂ consumption. Energy expenditure was adjusted for mouse body weight. Data were analyzed as described (Tschöp et al., 2011).

IEC and IEL isolation

IECs were isolated using an adapted protocol from Gracz et al. (2012). Briefly, small intestinal tissue was collected, cut longitudinally, and washed two times in cold PBS before incubating in PBS containing 30 mM EDTA and 1.5 mM dithiothreitol for 20 min on ice. The tissue was then transferred to PBS containing 30 mM EDTA and incubated under constant stirring for 10 min at 37°C. The epithelium, containing IELs, was released from the basement membrane by shaking and a single cell suspension

was obtained by incubating in HBSS buffer (without calcium and magnesium) containing 5 U/ml Dispase (Corning) constantly stirring for 10 min at 37°C. The resulting suspension was supplemented with 5% FCS and 0.25 mg/ml of DNase I (Sigma-Aldrich), homogenized by inversion, and passed through a 70- μ m cell strainer. Finally, cells were washed with 3% FCS/PBS before staining for flow cytometry or resuspended in TRIzol reagent for RNA isolation.

FACS sorting and RNA-Seq analysis of IECs

CD45⁻ Epcam⁺ IECs were sorted from the SI of 8-wk-old *Maf^{ΔIEC}* and littermate *Maf^{fl/fl}* control mice using a BD FACSAria sorter (sorting strategy Fig. S2 A). RNA was isolated with the RNeasy Micro Kit from Qiagen according to the manufacturer's protocol. RNA libraries were generated and sequencing was performed by Novogene (Cambridge, UK). Three biological replicates of each genotype were sequenced. Raw sequence reads were mapped to the mouse GRCm38/mm10 genome with Hisat2 v2.0.5 (Kim et al., 2015). featureCounts v1.5.0-p3 (Liao et al., 2014) was used to count the reads numbers mapped to each gene, and differential gene expression analysis was performed using DESeq2 (Love et al., 2014). A cut-off (p adj-value <0.1) was applied for calling differentially expressed genes. Differential gene expression data were plotted as MA plots using Prism 9 software (GraphPad) and for selected genes as heatmaps using Morpheus software (Broad Institute). The RNA-Seq data have been deposited to the NCBI GEO platform (GSE199191).

Gene set enrichment analysis (GSEA)

GSEA was performed using the GSEA tool from the Broad Institute (Subramanian et al., 2005). Gene sets used in this study were taken from the Kyoto Encyclopedia of Genes and Genomes database or published studies (Haber et al., 2017; Moor et al., 2018; Atarashi et al., 2015).

Sample preparation for amino acid analysis

Samples were extracted with 100% ethanol containing a universally labeled 13C, 15N internal standard mix of free amino acids (40 μ g/ml; Cambridge Isotope Laboratories, Inc.; MSK-CAA). Serum samples were defrosted, diluted 1:5 with the extraction solvent, and agitated for 10 min at 1,000 rpm at room temperature (RT; Thermomix Eppendorf). For external calibration, a series of six dilutions (1:3) was prepared in 90% ethanol using a mix of amino acid standards (all from Sigma Aldrich at >98% purity) before addition of the extraction solvent at one-third the volume. All samples and standards were cooled on ice for 20 min before insoluble matter was removed by centrifugation (2 min, 4°C, 16,100 rcf). 70 μ l of the supernatant was transferred to HPLC vials or conical 96-well plates.

Amino acid liquid chromatography–mass spectrometry (LC-MS) and data analysis

Amino acids were resolved on a Waters ACQUITY UPLCBEH Amide column (2.1 \times 100 mm, 1.7 μ m) using an Agilent 1290 HPLC with the flow directed to an Agilent 6470C triple quadrupole mass spectrometer operating in dynamic multiple reaction monitoring positive mode. The elution program (solvent A:

50:50 acetonitrile [ACN]/water, 10 mM NH₂COOH, 0.176% formic acid; solvent B: 95:5 ACN/MeOH/water, 10 mM NH₂COOH, 0.176% formic acid) was as follows: 85% B for 3 min before a linear gradient to 5% over 7 min, followed by a wash for 1 min (5% B) and column equilibration with 85% B for 1.7 min. Column temperature was 25°C, flow rate 0.6 ml/min, injection volume 1 µl, and the autosampler temperature controlled at 4°C. Precise source settings and multiple reaction monitoring transitions can be provided upon request. Compounds were identified by matching retention times and fragmentation patterns with analytical pure standards. Data analysis was performed with Agilent Masshunter software. Signals were integrated and quantified by calibrating with the ratios of natural to isotope-labeled internal standards and adjusted for dilution. Serum amino acid concentrations are reported in micromolars.

Sample preparation for proteomic analysis

IECs were resuspended in 100 µl radioimmunoprecipitation assay (RIPA) buffer with protease inhibitor and shaken at RT for 15 min (Eppendorf thermomixer) at 600 rpm. Mouse liver was homogenized in M-Tubes (130-093-236; Miltenyi Biotec) with 5 ml RIPA buffer and protease inhibitor in a GentleMacs instrument. 40 µl from the cell lysate plus 35 µl RIPA and 75 µl from tissue lysate were transferred to AFA-TUBE TPX 8-Strips (PN 520292) with caps (PN 500639). Samples were treated in a Covaris LE220Rsc to shear DNA (temperature 20°C, duty factor 25%, and plate definition dithering 1 mm Y-dither @ 20 mm/s; peak power 350, 300 s duration, two repeats). The protein concentration was determined (23225; Pierce Protein Assay Kit), and a volume corresponding to 25 µg was transferred to a TwinTec plate (Eppendorf), topped up to 50 µl with RIPA before SP3 protein digestion on a Beckmann Biomek i7 workstation as previously described with one-step reduction and alkylation (Muller et al., 2020). Briefly, 16.6 µl of reduction and alkylation buffer (40 mM Tris(2-carboxyethyl)phosphine hydrochloride, 160 mM chloroacetamide, 200 mM ammonium bicarbonate, 4% SDS) was added and the samples were incubated at 95°C for 5 min. Protein was bound to paramagnetic beads (1:1 mix of GE Healthcare, PN 45152105050250, 65152105050250) at a bead to protein ratio of 10:1 (wt/wt) with ACN at a final concentration of 50%. The samples were incubated for 18 min before placing on a magnetic rack for 3 min to pull down the beads with protein. The supernatant was discarded and the sample was washed twice with 80% ethanol and once with 100% ACN before reconstitution in 35 µl 100 mM ammonium bicarbonate. Trypsin/LysC (V5072; Promega) was added at an enzyme to protein ratio of 1:50 (wt/wt) and the samples were incubated at 37°C for 17 h (MP4; Benchmark Scientific Incu-Mixer). The reaction was stopped by adding formic acid to a final concentration of 0.1%. Peptide concentration was determined (23290; Pierce) and samples transferred to a new plate and frozen at -80°C until analysis by LC-MS/MS without further conditioning or cleanup.

Proteomics LC-MS

Peptide separation was accomplished in a 100-min water to acetonitrile gradient (solvent A: 0.1% formic acid [85178; Pierce] in LC-MS-grade water; solvent B: 0.1% formic acid in 80%

acetonitrile) on an Ultimate 3000 RSLnanoHPLC coupled to a Q-Exactive Plus mass spectrometer (Thermo Fisher Scientific) operating in data-independent acquisition (DIA) mode. 1.25 µg of peptides were concentrated on a trap column (PepMap C18, 5 mm × 300 µm × 5 µm, 100 Å; Thermo Fisher Scientific, buffer containing 2:98 [vol/vol] acetonitrile/water containing 0.1% [vol/vol] trifluoroacetic acid, flow rate of 20 µl/min) for 3 min and separated on a C18 column (Acclaim PepMap C18, 2 µm; 100 Å; 75 µm; Thermo Fisher Scientific, gradient flow rate 200 nl) in a linear gradient from 5 to 28% buffer B for 63 min followed by 28–95% B in 2 min and washing for 5 min with 95% buffer B before equilibration for 20 min with initial conditions flow 300 nl. The Orbitrap worked in centroid mode with a duty cycle consisting of one MS1 scan at 70,000 resolution with maximum injection time 300 ms and 3e6 AGC target followed by 40 variable MS2 scans using an 0.5Th overlapping window pattern. The window length started with 25 MS2 scans at 12.5 daltons; followed by seven windows with 25 daltons and eight windows at 62.5 daltons. Precursor MS spectra (m/z 378–1,370) were analyzed at 17,500 resolution after 110 ms accumulation of ions to a 3e6 target value in centroid mode. The background ions m/z 391.2843 and 445.1200 were used as lock mass. MS source settings were as follows: spray voltage 2.0 kV; no sheath and auxiliary gas flow; heated capillary temperature at 275°C; and normalized HCD collision energy 27%.

Proteomics data analysis

The raw data was processed using DIA-NN 1.8 (Demichev et al., 2020) with the ion mobility module for diaPASEF (Demichev et al., 2021 Preprint). MS2 and MS1 mass accuracies were both set to 15 ppm and the scan window size was automatically optimized. DIA-NN was run in library-free mode with standard settings (fasta digest and deep learning-based spectra, retention time and ion mobility prediction) using the Uniprot mouse reviewed (Swiss-Prot, downloaded on 2021-01-27) annotations (UniProt Consortium, 2019) and the match-between-runs option. Peptide normalized intensities were subjected to quality control with all samples passing acceptance criteria. Peptides with excessive missing values (>34 % per group) were excluded from analysis. The missing values of remaining peptides were imputed group-based using the PCA method (Josse and Husson, 2016). Normalization was performed with LIMMA (Ritchie et al., 2015) implementation of cyclic loess method (Bolstad et al., 2003) with option “fast” (Ballman et al., 2004). To obtain a quantitative protein data matrix, the log₂-intensities of peptides were filtered, and only peptides belonging to one protein group were kept and then summarized into protein log intensity by “PLM” method (Cox et al., 2014), implemented in R package preprocessCore (Pham et al., 2020). Statistical analysis of proteomics data was carried out using internally developed R scripts based on publicly available packages. Linear modeling was based on the R package LIMMA (Ritchie et al., 2015). The following model was applied to each tissue data set (log₂ transformed expression of a protein): log(p) ~ 0 + Class. The categorical factor Class had two levels: Ctrl and Ma^{AIIEC}. For finding regulated features, the following criteria were applied: significance level α was set to 0.01, which guaranteed for

contrast Ctrl vs. *Maf*^{ΔIEC} IECs, and the Benjamini–Hochberg (Benjamini and Hochberg, 1995) FDR <30%. The log fold-change criterion was applied to guarantee that the measured signal is above the average noise level. As such we have taken the median residual SD of linear model: $\log_2(T) = \text{median residual SD of linear modeling} (= \log_2[1.18])$. Functional GSEA analysis was carried out using R package clusterProfiler (Yu et al., 2012). For selecting the most (de)regulated GO terms, we applied filter: $10 \leq \text{term size} \leq 500$. The mass spectrometry proteomics data have been deposited to the ProteomeXchange Consortium via the PRIDE (Perez-Riverol et al., 2022) partner repository with the dataset identifier PXD034829.

Oral glucose administration

Maf^{ΔIEC} and littermate control mice were fasted for 7 h with water ad libitum. Then the body weight of the mice was measured and a total volume (in μl) of $7.5 \times \text{body weight (in grams)}$ of sterile 20% glucose (in PBS) was administered via oral gavage. The amount of glucose in blood was measured before and 30 and 60 min after gavage with a glucometer (ACCU-CHEK Mobile).

Feeding of purified diets

For diet experiments, *Maf*^{ΔIEC} littermate control mice were fed with specific isocaloric diets (“High protein” and “Low protein,” purchased from Ssniff) for 3 wk before analysis.

LP cell isolation

SI tissue was treated with HBSS buffer (without calcium and magnesium) containing 5 mM EDTA and 10 mM Hepes (pH 7.5) at 37°C for 30 min to remove epithelial cells, minced, and digested in HBSS buffer (with calcium and magnesium) containing 10 mM Hepes, 4% FCS, 0.5 mg/ml collagenase D, 0.5 mg/ml DNaseI (Sigma-Aldrich), and 0.5 U/ml Dispase (Corning) with constant stirring at 37°C for 30 min. The supernatant was filtered, and the remaining tissue was mashed through a 70- μm mesh. siLP cells were separated using a 40/80% step-gradient (Percoll solution; GE Healthcare). Recovered cells were counted and stained with different antibodies (Table S4). For cytokine analysis, cells were restimulated with PMA (Sigma-Aldrich, 10 ng/ml), ionomycin (Sigma-Aldrich, 1 $\mu\text{g/ml}$), and IL-23 (50 ng/ml) for 4 h in TexMACS medium (Miltenyi Biotec) containing 10% FCS. After 1 h of stimulation, Brefeldin A (Sigma-Aldrich, 5 $\mu\text{g/ml}$) was added to block cytokine secretion.

Flow cytometry

For flow cytometry, cells were stained with surface antibodies including a viability dye suitable for fixation if required at 4°C for 20 min. ILC3s were defined as viable CD45⁺ Lin⁻ CD127⁺ KLRG1⁻ NK1.1⁻ cells. Lineage includes anti-CD5, anti-CD8 α , anti-CD3, anti-Gr-1, anti-TCR $\gamma\delta$, anti-Fc ϵ RI α , anti-CD19, and anti-CD11c. For intracellular staining of cytokines and transcription factors, cells were fixed in Fix/Perm buffer (eBioscience) at 4°C for 1 h, followed by permeabilization (eBioscience) at 4°C for 2 h in the presence of antibodies. Cells were acquired with a BD LSRFortessa X-20, and analysis was performed with FlowJo (Tree Star) software.

FITC-Cystine uptake assay

To measure the uptake of Cystine by primary epithelial cells, IECs were isolated as described above and incubated with 5 μM BioTracker FITC-Cystine (Sigma-Aldrich) for 15 min in PBS. Then cells were stained with surface antibodies containing a viability dye, and EpCAM⁺ FITC-Cystine⁺ cells were measured by flow cytometry.

Whole-tissue FITC-Cystine and D-Ala-Lys-AMCA uptake assay

The SI was isolated from *Maf*^{ΔIEC} and littermate control mice. Afterward, a section of 7 cm of distal small intestine was longitudinally cut and thoroughly washed in cold PBS followed by incubation in PBS containing 5 μM BioTracker FITC-Cystine (Sigma-Aldrich) for 15 min or 25 μM D-Ala-Lys-AMCA (Hycultec) for 10 min at 37°C with constant horizontal agitation at 120 rpm. Then, SI tissue was washed three times in PBS, and Swiss rolls were prepared and fixed in 4% PFA as described below (see Materials and methods: IF staining). Finally, nuclei were stained with DAPI for 30 min at RT in combination with FITC-Cystine assay, or with Helix NP Green (BioLegend) for 15 min at RT in combination with D-Ala-Lys-AMCA assay. Images were taken on a Zeiss Axio Observer 7 (Carl Zeiss) and analyzed with ImageJ.

Organoid culture

For organoid cultures, 20 cm of the proximal SI was collected, cut longitudinally, and washed two times with cold PBS. The tissue was cut into 2-mm pieces, placed in cold PBS containing 5 mM EDTA, and pipetted up and down 10 times with a disposable pipette coated with 0.1% BSA/PBS. Then supernatant was discarded, and the tissue was incubated twice in 5 mM EDTA in PBS for 10 and 30 min at 4°C with constant agitation. After EDTA solution removal, fresh PBS was added and the tissue was pipetted up and down 15 times with a disposable pipette coated with 0.1% BSA/PBS, and the supernatant was collected in cold sterile RPMI medium. This procedure was repeated four more times to obtain a total of five fractions. The fraction with higher crypt enrichment was identified under the microscope and passed through a 70- μm cell strainer. Then crypts were counted and seeded on a 24- or 48-well plate at a density of 80 crypts/well in Matrigel (Corning). After polymerization was achieved by incubation for 30 min at 37°C, ENR medium was added (Advanced DMEM/F12 [Thermo Fisher Scientific] supplemented with 10 mM Hepes, 1 \times B27, 1 \times N2, 1 mM N-acetylcysteine [Sigma-Aldrich], 2 mM L-glutamine [Thermo Fisher Scientific], 100 $\mu\text{g/ml}$ penicillin/streptomycin, 50 ng/ml EGF [Thermo Fisher Scientific], 100 ng/ml Noggin [Peprotech], and 500 ng/ml murine R-spondin1 [R&D]) and refreshed every 2 d. Crypts were cultured at 37°C in 5% CO₂. For Noggin removal experiments, organoids were cultured in ENR medium for 2 d and then ENR was substituted for ER (ENR without Noggin). For stimulation with BMP-4, ENR or ER medium were supplemented with 100 ng/ml BMP-4 (Peprotech) and added to the culture for 6 h before organoids were resuspended in 500 μl Trizol (Life Technologies) and homogenized using MP FastPrep-24 (MP Biomedicals) for posterior RNA isolation.

Organoid crypt expansion index

For crypt expansion index, images of *Ma^f^{ΔIEC}* and control organoids were taken for 4 consecutive days after seeding. Buds and total organoids were then counted (at least 40 organoids per well) using ImageJ software, and crypt expansion index was calculated and shown as the number of crypts per organoid.

RNA isolation

mRNA from sorted cells was isolated with the RNeasy Plus Micro Kit according to the manual of the manufacturer (QIAGEN). RNA from cell suspensions, organoids, or tissues was extracted using TRIzol reagent following the protocol from ImmGen (Heng et al., 2008). The isolated RNA was quantified using Nanodrop 2000 before qPCR performance.

IF staining

For IF staining, 5–7 cm of the distal jejunum were taken and Swiss rolls were prepared as previously described with minor adaptations (Bialkowska et al., 2016). Briefly, Swiss rolls were fixed in 1% BD Cytofix/Cytoperm buffer in PBS for c-Maf, Slc15a1 (PEPT1), and Slc5a1 (SGLT1) staining or 4% PFA for DCLK1, ChgA, and UEA1 staining overnight at 4°C. After fixation, Swiss rolls were incubated in 30% sucrose in PBS overnight, embedded in O.C.T. Compound (Tissue-Tek, Sakura), and frozen with liquid nitrogen. O.C.T. blocks were cut into 5-μm sections for IF or conventional periodic acid-Schiff staining. For c-Maf, DCLK1, ChgA, and UEA1 staining, first, slides were rehydrated in cold PBS, then blocked and permeabilized in 0.5% Triton X-100 in PBS containing 10% Donkey serum (blocking buffer) at RT for 1 h and then incubated with primary antibodies (DCLK1, ChgA, and UEA1) in blocking buffer at RT for 1 h. Next, slides were incubated with c-Maf antibody in blocking buffer at RT overnight. For PEPT1 and SGLT1 staining, after rehydration of the slides in cold PBS, heat-induced epitope retrieval in Tris-EDTA buffer (pH = 9) for PEPT1 or in citrate buffer (pH = 6; Dako) for SGLT1 at 95°C for 20 min was performed. Then slides were cooled down at RT for 30 min and washed three times in PBS and blocked and permeabilized in blocking buffer at RT for 1 h. Next, primary antibody staining was performed at RT for 1 h in blocking buffer. Finally, slides were stained with secondary antibodies and DAPI in blocking solution at RT for 1 h and mounted with ProLong Diamond Antifade Mountant (Thermo Fisher Scientific). Images were taken on a confocal microscope LSM780 (Carl Zeiss), a Zeiss Axio Observer 7 (Carl Zeiss), and analyzed with ImageJ.

SFB quantification

For the quantification of SFB, ileal mucosal DNA was isolated. To specifically isolate the DNA from ileal mucosa, 2 cm of the ileum was taken, cut longitudinally, and washed thoroughly in cold PBS to remove the fecal content. The clean tissue was washed thoroughly in 0.1% Tween 80 in PBS, and the resulting solution was collected and spun down at 4°C, 16,000 g for 20 min to pellet the mucosal content. Bacterial DNA was then isolated from mucosal content with the ZymoBIOMICS DNA Miniprep Kit (Zymo Research), and bacterial load was measured by qPCR. The SFB abundance is presented relative to the abundance of eubacteria.

FISH of SFB

RNA-FISH for SFB was performed as previously described (Johansson and Hansson, 2012). Briefly, 5 cm of the ileum was fixed in Methacarn solution (60% absolute methanol, 30% chloroform, and 10% glacial acetic acid), paraffin-embedded, and cut into sections of 8 μm. Then slides were rehydrated and stained with 1 μg/μl of an SFB-specific 16S Cy3-labeled probe (5'-GCGAGCTTCCCTCATTACAAGG-3') in hybridization buffer (0.9 M NaCl, 20 mM Tris-HCl [pH 7.4], 0.1% SDS) at 50°C overnight. Finally, slides were counterstained with 1 μg/ml DAPI and mounted in ProLong Diamond Antifade Mountant (Thermo Fisher Scientific). Images were taken on Zeiss Axio Observer 7 (Carl Zeiss) and processed using ImageJ.

qPCR analysis

Total reverse transcription of isolated RNA was done with the High Capacity cDNA Reverse Transcription Kit (Applied Biosystems) as it is described in the manufacturer's protocol. qPCR was performed using a Quant Studio 5 system (Applied Biosystems) and the SYBR Green PCR Master Mix Kit (Applied Biosystems). The mRNA expression is presented relative to the expression of the housekeeping gene hypoxanthine-guanine phosphoribosyltransferase. Real-time qPCR primer used in this study can be found in Table S3.

Antibodies

A list of antibodies used in this study is provided in Table S4.

Statistical analysis

Data are represented as the means with SEM and summarize or are representative of independent experiments as specified in the text. Statistical analysis was performed using Prism 9 software (GraphPad) with two-tailed unpaired Student's *t* test (except RNA-Seq data).

Online supplemental material

Fig. S1 shows data, which demonstrate that intestinal epithelial c-Maf expression is driven by BMP signaling. Fig. S2 confirms that the expression of epithelial carbohydrate and protein transporters is reduced in *Ma^f^{ΔIEC}* mice. Fig. S3 shows that c-Maf-deficient organoids also express reduced levels of carbohydrate and protein transporters. Table S1 shows DE genes between c-Maf-deficient and control IECs as identified by RNA-Seq. Table S2 shows differentially expressed proteins between c-Maf-deficient and control IECs and liver tissue as identified by proteomics. Table S3 shows real-time qPCR primers used in this study. Table S4 lists all antibodies used in this study.

Acknowledgments

We thank Andreas Diefenbach (Charité – Universitätsmedizin Berlin, Germany) for discussion, providing key resources, and proofreading the manuscript. We further thank Efsthios Stamatides, Stylianos Gnafakis, Omer Shomrat, Manuela Stäber, Kathrin Textoris-Taube, Roodline Cineus, Ahmed Hegazy, and Frederik Heinrich for resources and technical and experimental help. The Benjamin Franklin Flow Cytometry Facility and the

Core Facility High Throughput Mass Cytometry at Charité – Universitätsmedizin Berlin are greatly acknowledged for cell sorting and proteomics analysis, respectively. In addition, we thank Dr. Anja A. Kühl and the iPATH facility at Charité – Universitätsmedizin Berlin for support in the preparation of histological samples and staining, the Central Biobank Charité – Universitätsmedizin Berlin for slide scanning and digitalization, and Jörg Piontek for technical support with confocal microscopy.

This research was supported by the Deutsche Forschungsgemeinschaft Priority Program 1937 (to C. Neumann), by the Ministry of Education and Research as part of the National Research Node "Mass spectrometry in Systems Medicine" under grant agreement 03IL0220 (to M. Ralser), the German Research Foundation (INST 335/797-1), and the Berlin University Alliance (501_Massenspektrometrie, 501_Linklab).

Author contributions: C. Cosovanu designed and performed most experiments, analyzed data, generated figures, and helped writing the manuscript. P. Resch helped with experimental design and execution. S. Jordan assisted in feeding experiments. A. Lehmann was responsible for sample preparation for metabolomics and LC-MS instrumentation. M. Ralser provided funding for personnel and analytical instruments. V. Farztdinov performed bioinformatic data analysis and presentation of proteomic data. M. Mülleder supervised MS measurements and was responsible for MS data analysis and management. J. Spranger and S. Brachs supervised metabolic analysis (NMR, metabolic cages) and provided reagents and equipment for their execution. C. Neumann conceived the project, designed and performed experiments, analyzed data, generated figures, and wrote the manuscript. All coauthors read, commented on, and approved the manuscript.

Disclosures: The authors declare no competing interests exist.

Submitted: 8 February 2022

Revised: 20 June 2022

Accepted: 24 August 2022

References

Aschenbrenner, D., M. Foglierini, D. Jarrossay, D. Hu, H.L. Weiner, V.K. Kuchroo, A. Lanzavecchia, and S. Notarbartolo, and F. Sallusto. 2018. An immunoregulatory and tissue-residency program modulated by c-MAF in human TH17 cells. *Nat. Immunol.* 19:1126–1136. <https://doi.org/10.1038/s41590-018-0200-5>

Atarashi, K., T. Tanoue, M. Ando, N. Kamada, Y. Nagano, S. Narushima, W. Suda, A. Imaoka, H. Setoyama, T. Nagamori, et al. 2015. Th17 cell induction by adhesion of microbes to intestinal epithelial cells. *Cell.* 163: 367–380. <https://doi.org/10.1016/j.cell.2015.08.058>

Ballman, K.V., D.E. Grill, A.L. Oberg, and T.M. Therneau. 2004. Faster cyclic loess: Normalizing RNA arrays via linear models. *Bioinformatics.* 20: 2778–2786. <https://doi.org/10.1093/bioinformatics/bth327>

Baulies, A., N. Angelis, and V.S.W. Li. 2020. Hallmarks of intestinal stem cells. *Development.* 147:dev182675. <https://doi.org/10.1242/dev.182675>

Benjamini, Y., and Y. Hochberg. 1995. Controlling the false discovery rate: A practical and powerful approach to multiple testing. *J. Roy. Stat. Soc. B (Methodological).* 57:289–300. <https://doi.org/10.1111/j.2517-6161.1995.tb02031.x>

Bialkowska, A.B., A.M. Ghaleb, M.O. Nandan, and V.W. Yang. 2016. Improved Swiss-rolling technique for intestinal tissue preparation for immunohistochemical and immunofluorescent analyses. *J. Vis. Exp.* 54161. <https://doi.org/10.3791/54161>

Bolstad, B.M., R.A. Irizarry, M. Astrand, and T.P. Speed. 2003. A comparison of normalization methods for high density oligonucleotide array data based on variance and bias. *Bioinformatics.* 19:185–193. <https://doi.org/10.1093/bioinformatics/19.2.185>

Burclaff, J., R.J. Bliton, K.A. Breaux, M.T. Ok, I. Gomez-Martinez, J.S. Ranek, A.P. Bhatt, J.E. Purvis, J.T. Woosley, and S.T. Magness. 2022. A proximal-to-distal survey of healthy adult human small intestine and colon epithelium by single-cell transcriptomics. *Cell Mol. Gastroenterol. Hepatol.* 13:1554–1589. <https://doi.org/10.1016/j.jcmgh.2022.02.007>

Cox, J., M.Y. Hein, C.A. Lubner, I. Paron, N. Nagaraj, and M. Mann. 2014. Accurate proteome-wide label-free quantification by delayed normalization and maximal peptide ratio extraction, termed MaxLFQ. *Mol. Cell. Proteomics.* 13:2513–2526. <https://doi.org/10.1074/mcp.M113.031591>

Crawley, S.W., M.S. Mooseker, and M.J. Tyska. 2014. Shaping the intestinal brush border. *J. Cell Biol.* 207:441–451. <https://doi.org/10.1083/jcb.201407015>

Dahl, W.J., D. Rivero Mendoza, and J.M. Lambert. 2020. Diet, nutrients and the microbiome. *Prog. Mol. Biol. Transl. Sci.* 171:237–263. <https://doi.org/10.1016/bs.pmbts.2020.04.006>

Demichev, V., C.B. Messner, S.I. Vernardis, K.S. Lilley, and M. Ralser. 2020. DIA-NN: Neural networks and interference correction enable deep proteome coverage in high throughput. *Nat. Methods.* 17:41–44. <https://doi.org/10.1038/s41592-019-0638-x>

Demichev, V., F. Yu, G.C. Teo, L. Szyrwiel, G.A. Rosenberger, J. Decker, S. Kaspar-Schoenefeld, K.S. Lilley, M. Mülleder, A.I. Nesvizhskii, and M. Ralser. 2021. High sensitivity Dia-PASEF proteomics with DIA-NN and FragPipe. *bioRxiv.* (Preprint Posted March 09, 2021). <https://doi.org/10.1101/2021.03.08.434385>

Diamond, J.M., and W.H. Karasov. 1987. Adaptive regulation of intestinal nutrient transporters. *Proc. Natl. Acad. Sci. USA.* 84:2242–2245. <https://doi.org/10.1073/pnas.84.8.2242>

El Marjou, F., K.P. Janssen, B.H. Chang, M. Li, V. Hindie, L. Chan, D. Louvard, P. Chambon, D. Metzger, and S. Robine. 2004. Tissue-specific and inducible Cre-mediated recombination in the gut epithelium. *Genesis.* 39: 186–193. <https://doi.org/10.1002/gene.20042>

Feliúbadalo, L., M.L. Arbones, S. Manas, J. Chillaron, J. Visa, M. Rodes, F. Rousaud, A. Zorzano, M. Palacin, and V. Nunes. 2003. Slc7a9-deficient mice develop cystinuria non-I and cystine urolithiasis. *Hum. Mol. Genet.* 12:2097–2108. <https://doi.org/10.1093/hmg/ddg228>

Gebert, N., C.W. Cheng, J.M. Kirkpatrick, D. Di Fraia, J. Yun, P. Schadel, S. Pace, G.B. Garside, O. Werz, K.L. Rudolph, et al. 2020. Region-specific proteome changes of the intestinal epithelium during aging and dietary restriction. *Cell Rep.* 31:107565. <https://doi.org/10.1016/j.celrep.2020.107565>

González-Loyola, A., J. Bernier-Latmani, I. Roci, T. Wyss, J. Langer, S. Durot, O. Munoz, B. Prat-Luri, M. Delorenzi, M.P. Lutolf, et al. 2022. c-MAF coordinates enterocyte zonation and nutrient uptake transcriptional programs. *J. Exp. Med.* <https://doi.org/10.1084/jem.20212418> 0022-1007

Gracz, A.D., B.J. Puthoff, and S.T. Magness. 2012. Identification, isolation, and culture of intestinal epithelial stem cells from murine intestine. *Methods Mol. Biol.* 879:89–107. https://doi.org/10.1007/978-1-61779-815-3_6

Groneberg, D.A., F. Doring, P.R. Eynott, A. Fischer, and H. Daniel. 2001. Intestinal peptide transport: Ex vivo uptake studies and localization of peptide carrier PEPT1. *Am. J. Physiol. Gastrointest. Liver Physiol.* 281: G697–G704. <https://doi.org/10.1152/ajpgi.2001.281.3.G697>

Haber, A.L., M. Biton, N. Rogel, R.H. Herbst, K. Shekhar, C. Smillie, G. Burgin, T.M. Delorey, M.R. Howitt, Y. Katz, et al. 2017. A single-cell survey of the small intestinal epithelium. *Nature.* 551:333–339. <https://doi.org/10.1038/nature24489>

Harnik, Y., L. Buchauer, S. Ben-Moshe, I. Averbukh, Y. Levin, A. Savidor, R. Eilam, A.E. Moor, and S. Itzkovitz. 2021. Spatial discordances between mRNAs and proteins in the intestinal epithelium. *Nat. Metabol.* 3: 1680–1693. <https://doi.org/10.1038/s42255-021-00504-6>

Heng, T.S.P., and M.W. Painter, and Immunological Genome Project Consortium. 2008. The immunological genome project: Networks of gene expression in immune cells. *Nat. Immunol.* 9:1091–1094. <https://doi.org/10.1038/ni1008-1091>

Hoffman, D.J., T.L. Powell, E.S. Barrett, and D.B. Hardy. 2021. Developmental origins of metabolic diseases. *Physiol. Rev.* 101:739–795. <https://doi.org/10.1152/physrev.00002.2020>

Hooton, D., R. Lentle, J. Monro, M. Wickham, and R. Simpson. 2015. The secretion and action of brush border enzymes in the mammalian small intestine. *Rev. Physiol. Biochem. Pharmacol.* 168:59–118. https://doi.org/10.1007/112_2015_24

Johansson, M.E., and G.C. Hansson. 2012. Preservation of mucus in histological sections, immunostaining of mucins in fixed tissue, and

- localization of bacteria with FISH. *Methods Mol. Biol.* 842:229–235. https://doi.org/10.1007/978-1-61779-513-8_13
- Josse, J., and F. Husson. 2016. missMDA: A package for handling missing values in multivariate data analysis. *J. Stat. Softw.* 70:1–31. <https://doi.org/10.18637/jss.v070.i01>
- Kikuchi, K., M. Iida, N. Ikeda, S. Moriyama, M. Hamada, S. Takahashi, H. Kitamura, T. Watanabe, Y. Hasegawa, K. Hase, et al. 2018. Macrophages switch their phenotype by regulating Maf expression during different phases of inflammation. *J. Immunol.* 201:635–651. <https://doi.org/10.4049/jimmunol.1800040>
- Kim, D., B. Langmead, and S.L. Salzberg. 2015. HISAT: A fast spliced aligner with low memory requirements. *Nat. Methods.* 12:357–360. <https://doi.org/10.1038/nmeth.3317>
- Kuwahara, T., Y. Ogura, K. Oshima, K. Kurokawa, T. Ooka, H. Hirakawa, T. Itoh, H. Nakayama-Imaohji, M. Ichimura, K. Itoh, et al. 2011. The life-style of the segmented filamentous bacterium: A non-culturable gut-associated immunostimulating microbe inferred by whole-genome sequencing. *DNA Res.* 18:291–303. <https://doi.org/10.1093/dnares/dsr022>
- Liao, Y., G.K. Smyth, and W. Shi. 2014. featureCounts: An efficient general purpose program for assigning sequence reads to genomic features. *Bioinformatics.* 30:923–930. <https://doi.org/10.1093/bioinformatics/btt656>
- Love, M.I., W. Huber, and S. Anders. 2014. Moderated estimation of fold change and dispersion for RNA-seq data with DESeq2. *Genome Biol.* 15: 550. <https://doi.org/10.1186/s13059-014-0550-8>
- Madison, B.B., L. Dunbar, X.T. Qiao, K. Braunstein, E. Braunstein, and D.L. Gumucio. 2002. Cis elements of the villin gene control expression in restricted domains of the vertical (crypt) and horizontal (duodenum, cecum) axes of the intestine. *J. Biol. Chem.* 277:33275–33283. <https://doi.org/10.1074/jbc.M204935200>
- Maier, T., M. Guell, and L. Serrano. 2009. Correlation of mRNA and protein in complex biological samples. *FEBS Lett.* 583:3966–3973. <https://doi.org/10.1016/j.febslet.2009.10.036>
- Mochizuki, K., K. Honma, M. Shimada, and T. Goda. 2010. The regulation of jejunal induction of the maltase-glucoamylase gene by a high-starch/low-fat diet in mice. *Mol. Nutr. Food Res.* 54:1445–1451. <https://doi.org/10.1002/mnfr.200900467>
- Moor, A.E., Y. Harnik, S. Ben-Moshe, E.E. Massasa, M. Rozenberg, R. Eilam, K. Bahar Halpern, and S. Itzkovitz. 2018. Spatial reconstruction of single enterocytes uncovers broad zonation along the intestinal villus Axis. *Cell.* 175:1156–1167 e15. <https://doi.org/10.1016/j.cell.2018.08.063>
- Muller, T., M. Kalxdorf, R. Longuespee, D.N. Kazdal, A. Stenzinger, and J. Krijgsveld. 2020. Automated sample preparation with SP3 for low-input clinical proteomics. *Mol. Syst. Biol.* 16:e9111. <https://doi.org/10.15252/msb.20199111>
- Neumann, C., J. Blume, U. Roy, P.P. Teh, A. Vasanthakumar, A. Beller, Y. Liao, F. Heinrich, T.L. Arenzana, J.A. Hackney, et al. 2019. c-Maf-dependent Treg cell control of intestinal TH17 cells and IgA establishes host-microbiota homeostasis. *Nat. Immunol.* 20:471–481. <https://doi.org/10.1038/s41590-019-0316-2>
- Pandit, T., V.K. Jidigam, and L. Gunhaga. 2011. BMP-induced L-Maf regulates subsequent BMP-independent differentiation of primary lens fibre cells. *Dev. Dyn.* 240:1917–1928. <https://doi.org/10.1002/dvdy.22692>
- Parker, M.E., A. Barrera, J.D. Wheaton, M.K. Zuberbuehler, D.S.J. Allan, J.R. Carlyle, T.E. Reddy, and M. Ciofani. 2020. c-Maf regulates the plasticity of group 3 innate lymphoid cells by restraining the type 1 program. *J. Exp. Med.* 217:e20191030. <https://doi.org/10.1084/jem.20191030>
- Perez-Riverol, Y., J. Bai, C. Bandla, D. Garcia-Seisdedos, S. Hewapathirana, S. Kamatchinathan, D.J. Kundu, A. Prakash, A. Frericks-Zipper, M. Eisenacher, et al. 2022. The PRIDE database resources in 2022: A hub for mass spectrometry-based proteomics evidences. *Nucleic Acids Res.* 50: D543–D552. <https://doi.org/10.1093/nar/gkab1038>
- Peterson, L.W., and D. Artis. 2014. Intestinal epithelial cells: Regulators of barrier function and immune homeostasis. *Nat. Rev. Immunol.* 14: 141–153. <https://doi.org/10.1038/nri3608>
- Pham, T.V., A.A. Henneman, and C.R. Jimenez. 2020. iq: An R package to estimate relative protein abundances from ion quantification in DIA-MS-based proteomics. *Bioinformatics.* 36:2611–2613. <https://doi.org/10.1093/bioinformatics/btz961>
- Prakash, T., K. Oshima, H. Morita, S. Fukuda, A. Imaoka, N. Kumar, V.K. Sharma, S.W. Kim, M. Takahashi, N. Saitou, et al. 2011. Complete genome sequences of rat and mouse segmented filamentous bacteria, a potent inducer of th17 cell differentiation. *Cell Host Microbe.* 10:273–284. <https://doi.org/10.1016/j.chom.2011.08.007>
- Ritchie, M.E., B. Phipson, D. Wu, Y. Hu, C.W. Law, W. Shi, and G.K. Smyth. 2015. Limma powers differential expression analyses for RNA-sequencing and microarray studies. *Nucleic Acids Res.* 43:e47. <https://doi.org/10.1093/nar/gkv007>
- Rutz, S., R. Noubade, C. Eidenschenk, N. Ota, W. Zeng, Y. Zheng, J. Hackney, J. Ding, H. Singh, and W. Ouyang. 2011. Transcription factor c-Maf mediates the TGF-beta-dependent suppression of IL-22 production in T(H)17 cells. *Nat. Immunol.* 12:1238–1245. <https://doi.org/10.1038/ni.2134>
- Szczesnak, A., N. Segata, X. Qin, D. Gevers, J.F. Petrosino, C. Huttenhower, D.R. Littman, and I Ivanov. 2011. The genome of th17 cell-inducing segmented filamentous bacteria reveals extensive auxotrophy and adaptations to the intestinal environment. *Cell Host Microbe.* 10: 260–272. <https://doi.org/10.1016/j.chom.2011.08.005>
- Seiler, K.M., S.E. Wayne, W. Kong, K. Kamimoto, A. Bajjanting, W.H. Goo, E.J. Onufer, C. Courtney, J. Guo, B.W. Warner, and S.A. Morris. 2019. Single-cell analysis reveals regional reprogramming during adaptation to massive small bowel resection in mice. *Cell Mol. Gastroenterol. Hepatol.* 8:407–426. <https://doi.org/10.1016/j.cmg.2019.06.001>
- Shibahara, T., J.N. Wilcox, T. Couse, and J.L. Madara. 2001. Characterization of epithelial chemoattractants for human intestinal intraepithelial lymphocytes. *Gastroenterology.* 120:60–70. <https://doi.org/10.1053/gast.2001.20904>
- Siska, P.J., B. Kim, X. Ji, M.D. Hoeksema, P.P. Massion, K.E. Beckermann, J. Wu, J.T. Chi, J. Hong, and J.C. Rathmell. 2016. Fluorescence-based measurement of cystine uptake through xCT shows requirement for ROS detoxification in activated lymphocytes. *J. Immunol. Methods.* 438: 51–58. <https://doi.org/10.1016/j.jim.2016.08.013>
- Subramanian, A., P. Tamayo, V.K. Mootha, S. Mukherjee, B.L. Ebert, M.A. Gillette, A. Paulovich, S.L. Pomeroy, T.R. Golub, E.S. Lander, and J.P. Mesirov. 2005. Gene set enrichment analysis: A knowledge-based approach for interpreting genome-wide expression profiles. *Proc. Natl. Acad. Sci. USA.* 102:15545–15550. <https://doi.org/10.1073/pnas.0506580102>
- Sullivan, Z.A., W. Khoury-Hanold, J. Lim, C. Smillie, M. Biton, B.S. Reis, R.K. Zwick, S.D. Pope, K. Israni-Winger, R. Parsa, et al. 2021. $\gamma\delta$ T cells regulate the intestinal response to nutrient sensing. *Science.* 371: eaba8310. <https://doi.org/10.1126/science.aba8310>
- Sumigray, K.D., M. Terwilliger, and T. Lechler. 2018. Morphogenesis and Compartmentalization of the Intestinal Crypt. *Dev. Cell.* 45:183–197.e5. <https://doi.org/10.1016/j.devcel.2018.03.024>
- Thibault, R., L. Genton, and C. Pichard. 2012. Body composition: Why, when and for who? *Clin. Nutr.* 31:435–447. <https://doi.org/10.1016/j.clnu.2011.12.011>
- Tizian, C., A. Lahmann, O. Holsken, C. Cosovanu, M. Kofoed-Branzk, F. Heinrich, M.F. Mashreghi, A. Kruglov, A. Diefenbach, and C. Neumann. 2020. c-Maf restrains T-bet-driven programming of CCR6-negative group 3 innate lymphoid cells. *Elife.* 9:e52549. <https://doi.org/10.7554/eLife.52549>
- Tschöp, M.H., J.R. Speakman, J.R. Arch, J. Auwerx, J.C. Bruning, L. Chan, R.H. Eckel, R.V. Farese Jr., J.E. Galgani, C. Hambly, et al. 2011. A guide to analysis of mouse energy metabolism. *Nat. Methods.* 9:57–63. <https://doi.org/10.1038/nmeth.1806>
- UniProt Consortium. 2019. UniProt: A worldwide hub of protein knowledge. *Nucleic Acids Res.* 47:D506–D515. <https://doi.org/10.1093/nar/gky1049>
- van Eijl, R.A.P.M., J.A.G.L. van Buggenum, S.E.J. Tanis, J. Hendriks, and K.W. Mulder. 2018. Single-cell ID-seq reveals dynamic BMP pathway activation upstream of the MAF/MAFB-Program in epidermal differentiation. *iScience.* 9:412–422. <https://doi.org/10.1016/j.isci.2018.11.009>
- Wang, Y., W. Song, J. Wang, T. Wang, X. Xiong, Z. Qi, W. Fu, X. Yang, and Y.G. Chen. 2020. Single-cell transcriptome analysis reveals differential nutrient absorption functions in human intestine. *J. Exp. Med.* 217: e20191130. <https://doi.org/10.1084/jem.20191130>
- Wende, H., S.G. Lechner, C. Cheret, S. Bourane, M.E. Kolanczyk, A. Pattyn, K. Reuter, F.L. Munier, P. Carroll, G.R. Lewin, and C. Birchmeier. 2012. The transcription factor c-Maf controls touch receptor development and function. *Science.* 335:1373–1376. <https://doi.org/10.1126/science.1214314>
- Xu, M., M. Pokrovskii, Y. Ding, R. Yi, C. Au, O.J. Harrison, C. Galan, Y. Belkaid, R. Bonneau, and D.R. Littman. 2018. c-MAF-dependent regulatory T cells mediate immunological tolerance to a gut pathobiont. *Nature.* 554:373–377. <https://doi.org/10.1038/nature25500>
- Yu, G., L.G. Wang, Y. Han, and Q.Y. He. 2012. clusterProfiler: An R package for comparing biological themes among gene clusters. *OMICS.* 16: 284–287. <https://doi.org/10.1089/omi.2011.0118>
- Zuberbuehler, M.K., M.E. Parker, J.D. Wheaton, J.R. Espinosa, H.R. Salzler, E. Park, and M. Ciofani. 2019. The transcription factor c-Maf is essential for the commitment of IL-17-producing $\gamma\delta$ T cells. *Nat. Immunol.* 20: 73–85. <https://doi.org/10.1038/s41590-018-0274-0>

Supplemental material

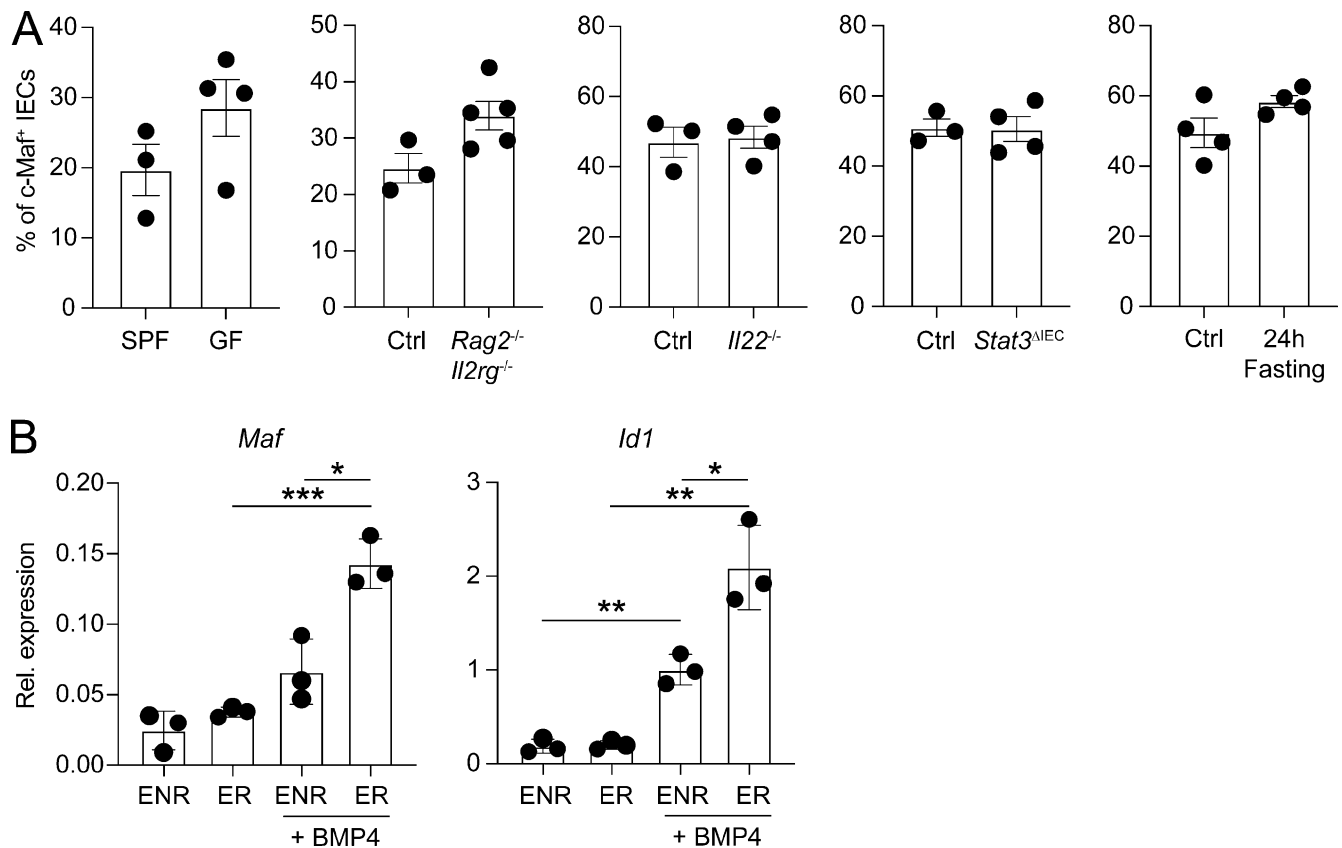


Figure S1. **Intestinal epithelial c-Maf expression is driven by BMP signaling.** **(A)** Frequency of c-Maf-expressing IECs in different mouse strains lacking key signals that extrinsically act on IECs, such as the microbiota (GF, germ free), immune cells (*Rag2*^{-/-} *Il2rg*^{-/-}), IL-22 (*Il22*^{-/-}), STAT3-activating cytokines (*Stat3*^{ΔIEC}), and diet (24-h fasting) as compared to respective controls ($n = 4$, mean \pm SEM). **(B)** SI organoid cultures from *Maf*^{ΔIEC} and littermate control mice were cultured in ENR medium for 2 d. Afterwards, ENR was refreshed or substituted for ER (ENR without Noggin) medium. In addition, organoids were stimulated with BMP-4 for 6 h at day 4 of culture before organoids were harvested for qPCR analysis. Graphs show relative expression of *Maf* and *Id1* ($n = 4$, mean \pm SEM; *, $P < 0.05$; **, $P < 0.01$; ***, $P < 0.001$). Data are representative of at least two independent experiments. Statistical differences were tested using an unpaired Student's *t* test (two-tailed).

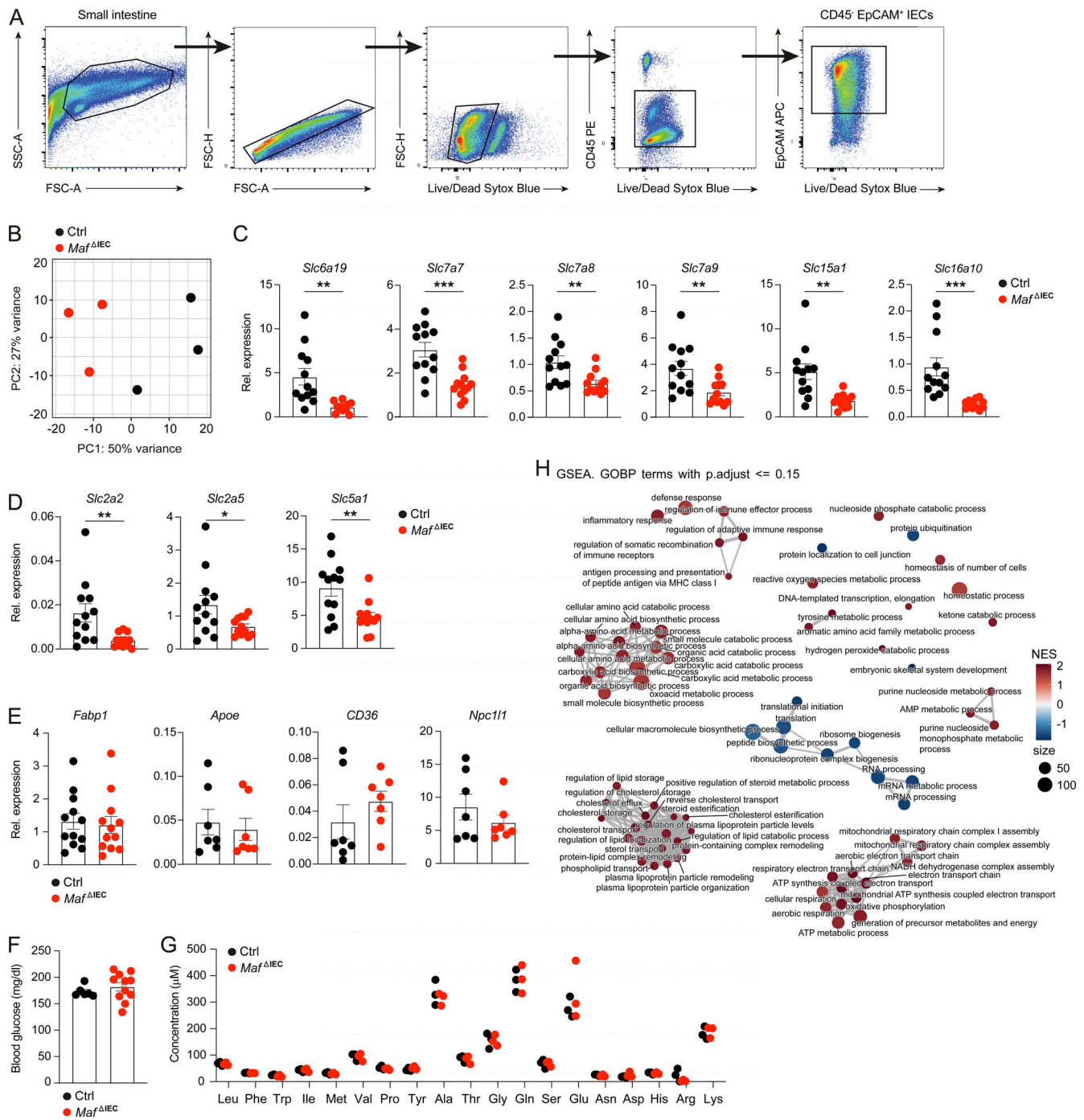


Figure S2. **Reduced expression of carbohydrate and protein transporters in *Maf*^{ΔIEC} mice.** (A) Gating strategy for FACS-sorting of SI IECs (CD45⁻ EpCAM⁺) for RNA-Seq analysis. Numbers in the plots indicate percentage. (B) RNA-Seq based PCA of FACS-sorted IECs. Each dot represents an individual biological replicate. (C) Relative expression of different amino acid and peptide transporters by IECs isolated from *Maf*^{ΔIEC} and control mice ($n = 12$, mean \pm SEM; **, $P < 0.01$; ***, $P < 0.001$). (D) Relative expression of different glucose transporters by IECs isolated from *Maf*^{ΔIEC} and control mice ($n = 12$, mean \pm SEM; *, $P < 0.05$; **, $P < 0.01$). (E) Relative expression of different genes important for lipid uptake by IECs isolated from *Maf*^{ΔIEC} and control mice ($n = 7-12$, mean \pm SEM). (F) Steady-state blood glucose level of *Maf*^{ΔIEC} and control mice ($n = 6-11$, mean \pm SEM). (G) Steady-state plasma amino acid concentrations of *Maf*^{ΔIEC} and control mice ($n = 3$). Data are pooled from at least two independent experiments. Statistical differences were tested using an unpaired Student's *t* test (two-tailed). (H) GSEA of whole proteome comparison between liver tissue isolated from *Maf*^{ΔIEC} and control mice with a focus on biological processes (GOBP). The size of each circle represents the weighted number of proteins involved in the term. NES, normalized enrichment score. Data represent the combined analysis of six and three biologically independent samples from control and *Maf*^{ΔIEC} mice, respectively.

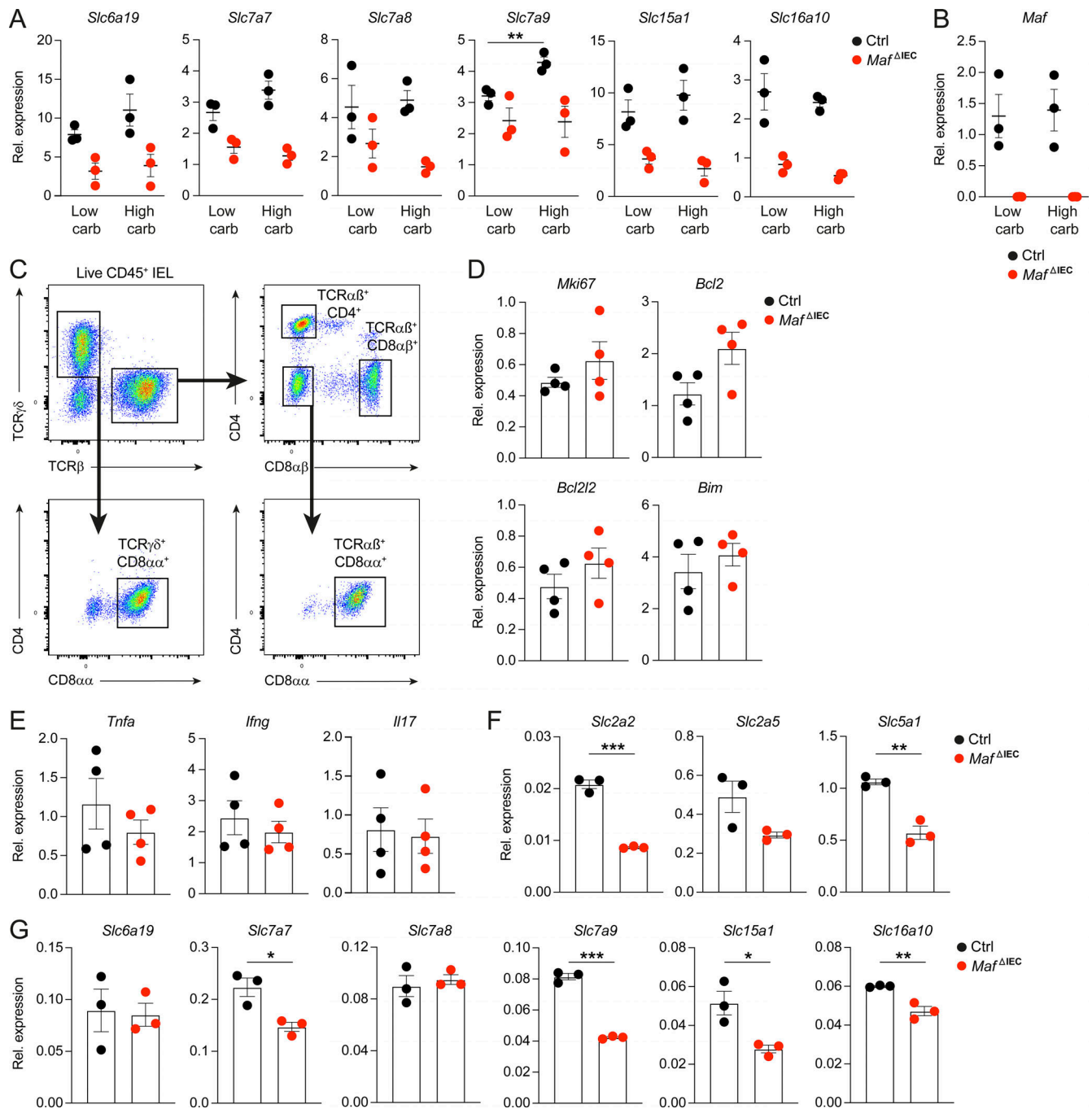


Figure S3. Reduced expression of carbohydrate and protein transporters in c-Maf-deficient organoids. (A and B) Relative expression of amino acid and peptide transporters and *Maf* by IECs from *Maf*^{ΔIEC} and control mice after 3 wk of feeding purified diets with high or low carbohydrate content ($n = 3$, mean \pm SEM; **, $P < 0.01$). (C) Gating strategy for flow cytometric analysis of SI IEL subsets. Numbers in the plots indicate percentage. (D) qPCR analysis of *Mki67*, *Bcl2*, *Bcl2l2*, and *Bim* in FACS-sorted SI IELs from *Maf*^{ΔIEC} and control mice ($n = 4$, mean \pm SEM). (E) qPCR analysis of *Tnfa*, *Ifng*, and *Il17* in FACS-sorted SI IELs from *Maf*^{ΔIEC} and control mice ($n = 4$, mean \pm SEM). (F and G) Relative expression of glucose, amino acid, and peptide transporters by SI organoids derived from *Maf*^{ΔIEC} and control mice ($n = 3$, mean \pm SEM; *, $P < 0.05$; **, $P < 0.01$; ***, $P < 0.001$). Data are representative of least two independent experiments. Statistical differences were tested using an unpaired Student's *t* test (two-tailed).

Provided online are four tables. Table S1 shows DE genes between c-Maf-deficient and control IECs as identified by RNA-Seq. Table S2 shows differentially expressed proteins between c-Maf-deficient and control IECs and liver tissue as identified by proteomics. Table S3 shows real-time qPCR primers used in this study. Table S4 lists all antibodies used in this study.